Powder Technology 429 (2023) 118962

Contents lists available at ScienceDirect

Powder Technology

journal homepage: www.journals.elsevier.com/powder-technology

Development of ceramic-MOF filters from aluminum saline slags for capturing CO_2

J.J. Torrez-Herrera, S.A. Korili, A. Gil *

INAMAT˜2-Departamento de Ciencias, Edificio de los Acebos, Universidad Pública de Navarra, Campus de Arrosadía, E-31006 Pamplona, Spain

HIGHLIGHTS

- Aluminum saline slags were used to prepare ceramic filters.
- Ceramic filters are used as supports of MOF structures.
- Ceramic-MOF filters as adsorbents of CO_2.

GRAPHICAL ABSTRACT

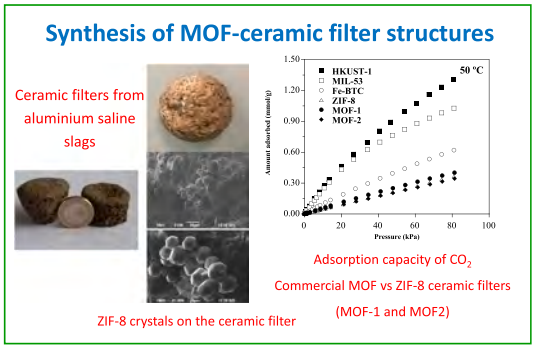

ARTICLE INFO

Keywords:
Aluminum industrial waste
Ceramic-MOF filter synthesis from saline slags
Carbon dioxide adsorption

ABSTRACT

This study describes the procedures followed to synthesize ceramic-MOF filters using aluminum saline slag wastes. Briefly, the raw aluminum saline slags were washed at 80 °C to significantly reduce the saline content and eliminate gases. The pretreated material was mixed with glucose (G/S ratios between 0.2 and 1.6) and acetone by stirring for 4 h. After this time, the resulting solid was dried at 60 °C and then at 190 °C. During the glucose caramelization step, PegMn400 was also added and the temperature increased to 1200 °C. The obtained solid was impregnated with precursor solutions to achieve a supported ZIF-8 MOF. The ceramic-MOF filters were characterized by X-ray diffraction (XRD), N_2 adsorption at 77 K, X-ray fluorescence (XRF), scanning electron microscopy (SEM) and transmission electron microscopy (HR-TEM), thereby confirming the presence of a structure that allows dispersion of the synthesized and supported ZIF-8. Finally, the performance of these ceramic-MOF filters as CO_2 adsorbents was evaluated in the temperature range 50–300 °C, with isosteric heats of 19 kJ/mol being obtained using the Clausius-Clapeyron equation.

1. Introduction

The 2030 Agenda for Sustainable Development, adopted by all United Nations Member States in 2015, provides a strategic plan for, among other things, the prosperity of people and the planet. In this agreement are the 17 Sustainable Development Goals (SDGs), which are an urgent call to action by all countries, developed and developing. In the case of the research work that we address here, the SDGs that are

* Corresponding author.
E-mail address: andoni@unavarra.es (A. Gil).

https://doi.org/10.1016/j.powtec.2023.118962
Received 25 July 2023; Received in revised form 25 August 2023; Accepted 4 September 2023
Available online 6 September 2023

addressed would be: ***SDG 9*** *Industry, innovation and infrastructure*. By including technology minimization/prevention measures, it would try to reduce CO_2 emissions through the development of adsorption processes; ***SDG 12*** *Responsible consumption and production.* Through the recovery of industrial waste, such as aluminum saline slags, it is possible to encourage sustainable practices and thus reduce the use of natural resources; ***SGD 13*** *Climate action*. Development of ceramic foams that could work as filters to reduce greenhouse gas emissions, in particular CO_2.

The adsorption of greenhouse gases such as CO_2 continues to arouse great interest among the scientific community due to its impact on climate change. CO_2 generation has increased by approximately 143% over the past few decades, mainly among five sectors: transport, industry, electricity generation, buildings and agriculture, which account for 45% of all emissions. Indeed, in the case of the combustion of fossil fuels, it is estimated that this process releases 32 Gt/year (1 Gigatonne (Gt) = 1 billion tonnes), which are the main source (80%) of CO_2. According to the EU, 0.03 Gt of CO_2 could be captured and stored by 2050 in Europe and, globally, this amount could reach 0.240 Gt [1–4]. However, it is necessary to increase the measures so that the capture and use processes are more effective. From here arises the development of Carbon Capture, Utilization and Storage (CCUS) technologies whose objective is to reduce/avoid biogenic and non-biogenic CO_2 emissions.

Greenhouse gas emissions, such as CO_2, accumulate heat on the earth's surface, which has an impact on an increase in its temperature. The Paris agreement established the objective of limiting the current increase in global temperatures to 2 °C, thus meaning that, for example, CO_2 emissions into the atmosphere must be reduced and adsorption technologies developed [5–8]. Efficient adsorption technologies depend on the development of adsorbents with textural, topological and morphological properties that allow optimal CO_2 storage with the best possible cost/benefit ratio. The most commonly used advanced physical adsorbents include activated carbons, zeolites and most metal–organic frameworks (MOFs) [9–13], which fix CO_2 in their structure as a result of van der Waals forces or electrostatic interactions. MOFs present significant potential for the capture, concentration and, ultimately, storage and transport of CO_2. Thus, it has been reported that a gas cylinder filled with MOF-177, which has a specific surface area of 4500 m^2/g, can capture and store nine times more CO_2 at room temperature than the same gas cylinder without the MOF [14,15].

MOFs represent one of the most important research fields due to their applicability in various areas, such as gas storage and adsorption, heterogeneous catalysis, biological treatments, biomedical applications and chemical sensors, among others [16]. These organometallic networks present large specific surface areas, with pore diameters ranging between 0.5 and 2.5 nm. Among these materials, there is a subgroup with a sodalite topology, known as ZIFs (zinc-imidazole (Im) frameworks), with interesting thermal stability and chemical properties. Typically, these materials exhibit structures similar to those of sodalite, which have a tetrahedral structure [Si(*Al*)O_4], with metals bound to the organic binder (Im) while maintaining the same distribution (M-Im-M) [17–19]. One of the most important ZIFs is ZIF-8 ($Zn(mim)_2$, mim = 2-methylimidazole), which has a typical sodalite-like structure and exhibits mechanical, structural and configurational properties that give it excellent thermal stability up to 400 °C and high specific surface areas [20–23]. The most important characteristics for the applications of ZIF-8 arise from morphological aspects of the particles, the growth of nano-microcrystals and the final forms obtained, which determine the flexibility of the structure and its catalytic and adsorbent performance. Many of these morphological and textural modifications are closely related to the synthesis methods used, the most common of which include: high-throughput, solvothermal, electrochemical, hydrothermal mechanochemical, microwave-assisted, template, sonochemical, atomic layer deposition, sol-gel, spray-drying, supercritical and chemical synthesis methods [23–37]. Of these, the two most widely used, due to their easy application, are solvothermal synthesis and room-temperature synthesis. Currently, the use of hybrid materials allows the possible applications and functionalities to vary widely. These materials, which have large specific surface areas and excellent stability, can be deposited in different materials and structures (alumina, carbon, ceramic sponges, alloys, composites, etc.) that allow fixing of the particles [38].

The second-generation aluminum industry generates a waste known as aluminum saline slag as a consequence of the large amounts of fluxing salts used. The composition of this slag varies slightly depending on the type of materials recycled [39,40]. Generally, this slag is composed of non-metallic oxides, salts, metallic aluminum and other trace compounds [41–45]. This material currently poses a serious problem for industry, since it is considered to be highly hazardous given the vapors it contains and generates in contact with water. As such, new ways to treat and reuse this waste to also obtain added value in the synthesis of new materials as a result of the extraction of metallic aluminum, are urgently required [39,42,44]. The materials synthesized using this slag includes alumina [44–47], hexaaluminates [48–50], zeolites [51–55], calcium aluminate [56–58], double-layered hydroxides [59–64], and molecular sieves, among others [65–67].

There are some reports of the use of saline slags as a foaming agent for the generation of glass–ceramic sponges from urban solid waste [68]. The physicochemical and mechanical properties of these sponges make them suitable to be used in several areas, such as wastewater and solid waste treatment, noise absorption and reduction, construction, metal casting and as catalysts for combustion gases in automobiles and catalytic supports, etc. [69–75]. From our knowledge, these materials could be applied directly in these applications or as a support for structures developed from industrial waste [13,40,49,60,63,64,67]. The most widely used methods to produce ceramic sponges include replication of polymeric foams, foaming and setting of ceramic powder suspensions, emulsion templates, and thermofoaming with sucrose and molten glucose [76–85]. Similarly, aluminas are some of the most common materials for the elaboration of ceramic sponges due to their properties and availability. Considering the mitigation of climate change, the reuse of hazardous waste and the potential of ZIF-8 and aluminum saline slags, the aim of this study was to develop a ceramic-MOF foam filter that brings together the most important qualities of both materials and results in a robust device for various applications. As a first objective of this work, a ceramic foam is synthesized from the aluminum saline slags. In order for the hazardous waste used to have mechanical resistance and to be used as a filter/support, it is necessary to add glucose and a surfactant. Once the ceramic foam was obtained, this material has been used as a support for ZIF-8, for which several procedures have been used that involve, on the one hand, impregnation with a ZIF-8 precursor and, on the other hand, the in-situ synthesis of ZIF-8. The ceramic-MOF filters thus obtained have been used as CO_2 adsorbents and their capacities have been compared with several commercial MOFs: MIL-53 (Basolite A100), HKUST-1 or Cu-BTC (Basolite C300), Fe-BTC (Basolite F300) and ZIF-8 (Basolite Z1200).

2. Experimental

2.1. Materials, reagents and gases

The materials and reagents used to synthesize the ceramic-MOF filters included $Zn(NO_3)_2{\cdot}6H_2O$ (99.9%, Sigma-Aldrich), 2-methylimidazole (Hmim) (99%, Sigma-Aldrich), anhydrous *N*,*N*-dimethylformamide (99.8%, DMF), methanol (99.8%, ACS), D (+)-glucose (99.5%, Sigma-Aldrich), acetone (ACS reagent, ≥99.5%, Aldrich), polyethylene glycol Monolaurate 400 (PegMn400, Aldrich) and aluminum saline slags (kindly supplied by IDALSA). Various commercial MOFs were used to compare CO_2 adsorption: MIL-53(Al) (Basolite A100, Sigma-Aldrich), which has a structure built up from infinite chains of corner-sharing $AlO_4(OH)_2$ octahedra connected via 1,4-benzenedicarboxylate ligands; HKUST-1 or Cu-BTC (Basolite C300, Sigma-Aldrich), which is a crystallized hybrid porous solid built up from

inorganic subunits connected to organic linkers such as carboxylates; Fe-BTC (Basolite F300, Sigma-Aldrich), which has a hybrid super-tetrahedral structure comprising oxo-centred trimmers of iron(III) octahedra connected via trimesate anions; and ZIF-8 (Basolite Z1200, Sigma-Aldrich), which comprises metal ions and imidazolate anions. Carbon dioxide (99.996%, Nippon Gases), nitrogen (99.999%, Nippon Gases) and helium (99.999%, Nippon Gases) were also used in the characterization and application studies.

2.2. Synthesis of ceramic foams from aluminum slags

Aluminum saline slags, which have a high content of alumina, salts (NaCl+KCl), magnesia and silica (see Table 1), were used as raw materials to synthesize the ceramic foams. These slags were subjected to a successive washing process at 80 °C under vigorous stirring, using the procedure described by Gil and Korili [43], which allows the salt content to be significantly reduced and also eliminates gases such as NH_3, H_2S, and CH_4, among others. The result is a clean saline slag whose chemical composition is summarized in Table 1.

Once the saline slags had been pretreated, mixtures with several weight ratios of these slags and glucose powders were prepared (100 g of saline slag as a constant base and glucose/slag (G/S) ratios between 0.2 and 1.6). These mixtures were placed in a ball mill with a porcelain body with a volume of 1500 cm^3 and unvitrified porcelain balls of several sizes (20 mm (60%), 15 mm (20%), 9 mm (20%)), for a total of 100 units. Acetone was added to each of the mixtures, as a liquid matrix, in a 1:1 ratio with the powder mixture, that is, 250 cm^3 for the 1.5 G/S mixture (250 g). The A:G:S (acetone:glucose:slag) mixture inside the mill was homogenized and compacted for 4 h to give a powder cake with a water content of 20–30 wt%. Subsequently, the wet powders were placed in an oven with an air atmosphere at 60 °C for 2 h. Once the powders had been dried, they were deposited in alumina ceramic molds, occupying between 60 and 70% of their maximum volume. The powders were compacted in the mold and placed in an oven at 190 °C for 10 min, manually mixing the sludge every 3 min until complete caramelization of the glucose was achieved. Then, 2–3 cm^3 of PegMn400 was added to the mixture, which was subsequently mechanically stirred to ensure complete incorporation of the polymer. Once cold, the resulting green glucose-slag-PegMn400 capsules were placed in the oven again at 170 °C for 45 min until complete swelling of the caramelized matrix had been achieved. After this step, the temperature was increased to 230 °C for 1 h, thus resulting in the solidification of the carbonaceous matrix of glucose in the green sponge. The temperature was subsequently increased again up to 700 °C (10 °C/min) and 1200 °C (2 °C/min), at a steady state of 2 h at both temperatures.

2.3. Synthesis of Zeolite Imidazolate Framework (ZIF-8)

The ZIF-8 compound was synthesized using two methods:

a) Room-temperature synthesis [86,87] (MOF-1). In this method, 9.87 mmol of $Zn(NO_3)_2{\cdot}6H_2O$ and 79.04 mmol of 2-methylimidazole (*Hmim*) were dissolved in 20 and 200 cm^3 of methanol, respectively, with vigorous stirring. Subsequently, 20 cm^3 of zinc nitrate-methanol solution was added dropwise to the *Hmim* solution at room temperature, and the mixture was sonicated for 30 min. After a few minutes, the mixture became more cloudy and a white slurry was obtained after 1 h. This slurry was centrifuged at 1500 rpm for 15 min and the MOF crystals washed with methanol and the sludge was then dried at 40 °C for 4 h.

b) Solvothermal synthesis [87] (MOF-2). In this second method, 2 mmol of $Zn(NO_3)_2{\cdot}6H_2O$ and 2 mmol of 2-methylimidazole (*Hmim*) were dissolved in 50 cm^3 of *N*,*N*-dimethylformamide with vigorous stirring to obtain a translucent solution. This solution was transferred into a 100 cm^3 Teflon-lined stainless-steel autoclave, which was placed in an oven at 140 °C for 24 h. The precipitate was then separated by centrifugation of the liquid matrix at 1500 rpm for 15 min and washed with methanol. The resulting MOF crystals were dried at 40 °C for 4 h.

2.4. Manufacture of the ceramic foam-ZIF-8

The two methods used to synthesize MOF-ZIF-8 were also used to impregnate the ceramic foam:

a) The ceramic foam, prepared using a glucose/slag ratio of 0.7, was treated to remove physisorbed gases, humidity and impurities, by adding it to a solution of acetone, methanol, isopropanol in a 1:1:1 ratio (150 cm^3). The beaker containing the solution was then placed in a sonicator for 30 min and subsequently dried at 90 °C for 1 h. After this first treatment, the solid was impregnated and mixed with the MOF–methanol solution (white slurry) and synthesized using the room-temperature method for 1 h with mechanical stirring. Subsequently, two rinses with methanol were performed to remove surface nanoparticles. The ceramic MOF-filter was placed in an oven at 100 °C for 1 h and then activated at 120 °C for 6 h.

A reference sample was also prepared using a commercial ZIF-8 (Basolite Z1200, Sigma-Aldrich). Thus, 200 mg of this powder was dissolved in 100 cm^3 of methanol to form a slurry saturated with nanoparticles of the zeolitic MOF, subsequently repeating the previous

Table 1
Chemical composition by FRX of the saline slags before (A) and after cleaning treatment (B), and of the ceramic foam prepared using a glucose/slag ratio of 0.7 (C).

(A)

Composition	**Na_2O**	**MgO**	**Al_2O_3**	**SiO_2**	**P_2O_5**	**SO_3**	**Cl**	**K_2O**	**CaO**
wt%	8.65	2.76	41.71	4.23	0.05	0.52	11.83	4.40	2.08
Composition	**TiO_2**	**Cr**	**MnO**	**Fe_2O_3**	**Ba**	**Cu**	**F**	**Zn**	
wt%	0.31	0.04	0.17	2.05	0.08	0.35	0.41	0.18	

(B)

Composition	**Na_2O**	**MgO**	**Al_2O_3**	**SiO_2**	**P_2O_5**	**SO_3**	**Cl**	**K_2O**	**CaO**
wt%	0.77	6.49	55.23	4.23	0.07	0.41	0.47	0.50	2.12
Composition	**TiO_2**	**Cr**	**MnO**	**Fe_2O_3**	**Ba**	**Cu**	**F**	**Zn**	
wt%	0.65	0.07	0.26	1.25	0.07	0.51	0.41	0.17	

(C)

Composition	**Na_2O**	**MgO**	**Al_2O_3**	**SiO_2**	**P_2O_5**	**Cl**	**K_2O**	**CaO**
wt%	0.41	4.64	75.49	8.20	0.06	0.2	0.26	2.26
Composition	**TiO_2**	**Cr**	**MnO**	**Fe_2O_3**	**Ba**	**Cu**	**Zn**	
wt%	0.7	0.11	0.27	4.15	0.18	0.58	0.27	

procedure.

b) In the second method, the treated ceramic support without physisorbed gases, humidity and impurities was added to a solution comprising 4 mmol of $Zn(NO_3)_2{\cdot}6H_2O$ and 4 mmol of 2-methylimidazole (Hmim) dissolved in 150 cm^3 of *N*,*N*-dimethylformamide. The solution and support were then transferred into a 500 cm^3 Teflon-lined stainless steel autoclave, which was placed in an oven at 140 °C for 24 h. After this time, a caramel-colored precipitate was obtained. The support was then washed twice with methanol and added to 150 cm^3 of n-hexane for 90 min. The resulting solid was dried at room temperature for 48 h, and then at 120 °C for 6 h.

2.5. Characterization

The structural phases were analyzed using an X-ray diffractometer (model Siemens D5000) equipped with an Ni-filtered CuKα radiation source ($\lambda = 0.1548$ nm). The crystallite size was determined from the experimental diffractograms using the Debye–Scherrer equation. The main textural properties of the solids were determined by N_2 adsorption at −196 °C using a Micromeritics ASAP 2020 Plus adsorption analyzer. Prior to the adsorption measurements, 0.3 g of sample was degassed at 200 °C for 2 h at pressures lower than 0.133 Pa. The BET specific surface area (S_{BET}) was calculated from nitrogen adsorption data obtained over the relative pressure range from 0.05 to 0.20. The total pore volume (V_P) was calculated from the amount of nitrogen adsorbed at a relative pressure of 0.99. The chemical compositions of the samples were determined semi-quantitatively by X-ray fluorescence (XRF) spectroscopy using a PANalytical AXIOS instrument. Finally, the morphological analysis and chemical composition of the samples were carried out by SEM (INSPECT F50, Mode: 30 kV - Map, Detector: BSD Full) and TEM (FEI Tecnai F30, Accelerating voltage: 200 kV, Detector: HAADF-STEM).

2.6. CO_2 adsorption

CO_2 adsorption was evaluated using a static volumetric method with a Micromeritics ASAP 2010 instrument and 0.3 g of solid. The samples were pre-treated at a heating rate of 10 °C/min, under a flow of He at 50 °C for 2 h and then heated to the adsorption temperature in the same stream. The samples were degassed under vacuum to a pressure of <0.6

Fig. 1. Ceramic foam prototypes made with two molds using the experimental process. 1-a) G/S paste (0.7 wt%) melted and homogenized inside a truncated conical ceramic mold for high temperatures 1-c). 2-a) cylindrical ceramic mold, 2-b)-c) green carbonaceous foam, 2-d) cylindrical prototype of the ceramic support filter at 1200 °C. (For interpretation of the references to colour in this figure legend, the reader is referred to the web version of this article.)

Pa at the adsorption temperature. CO_2 adsorption data were collected in the pressure range between 0.1 and 82 kPa.

3. Results and discussion

3.1. Characterization of aluminum saline slags and ceramic foam

The chemical composition of the aluminum saline slags before and after cleaning, and of the ceramic foam can be found in **Table 1**.

The ceramic foam supports obtained from the aluminum saline slags after the washing process, which had various shapes and sizes depending on the ceramic molds used, are summarized in Fig. 1. The two alumina molds for high temperatures, with dimensions $D_{A1} = 4.8$ mm, $D_{A2} = 2.2$ mm, $h_A = 4.2$ mm (**1c**) and $D_B = 5$ mm, $h_B = 6$ (**2a**), were used as an expansion vessel during the glucose decomposition. To obtain this solid, various G/S mass ratios were used, with G/S values >0.75, during the glucose melting/caramelization stage, giving a highly fluid syrup that resulted in a high foaming rate and prevented the control of sponge growth. Under these conditions, weak green foams and an overflow of the molds were observed. In contrast, at lower values (< 0.65), expansion of the slag due to foaming of the glucose syrup was ineffective and prevented the formation of interstices and growth of the solid matrix. The use of a small dose of PegMn400 as an adjuvant flux generated homogeneity and integration of the caramelized syrup and the saline slags. Several combinations of temperatures and melting-foaming times were used, performing inspections and mechanical stirring every 5–8 min until an integral and homogeneous matrix was obtained. Based on these data and results, it was possible to identify the optimal mass ratios and the process parameters that allowed us to control and obtain the prototypes, namely a mass ratio (G/S) of 0.7, a melting temperature and residence time of 190 °C and 30 min, respectively, and 3–5 cm^3 of PegMn400 flux. After glucose melting, the syrup was stirred mechanically with a glass rod and homogenized. The foaming temperature was 190 °C for 20–30 min, until an expansion of 30% in volume had been achieved, in air, followed by subsequent carbonization at 220 °C for 2 h, using an accelerated ramp of 50 °C/min from 190 to 220 °C, which allows the consistency of the foam to be maintained and prevents over-foaming of the mixture.

A series of composite images showing the evolution of the G/S powders with a 0.7 weight ratio after the maceration–grinding stage, using conical and cylindrical molds, can be found in Fig. 1. The saline slag powders and mixtures are presented in Fig. 1 (3)–(4). When applying the experimental process carried out, once the powders had been mixed and macerated, using acetone as a dispersive medium, and dried at 60 °C for 2 h, a mixture such as that shown in Fig. 1 (4) was obtained (light gray powder without agglomerates). The powders deposited in any of the molds of Fig. 1 [1-c), 2-a)] up to 45% of the h_{Total} were mechanically compacted and deposited in a muffle oven, with manual stirring, until the G/S base paste had melted and become homogeneous, as shown in Fig. 1 [1-a)], for subsequent caramelization, foaming and carbonization of the expanded paste. At the end of the sintering process for the green sponge, Fig. 1 [2-b), c)], the ceramic prototype shown in Fig. 1 [(1,2)-d)] sintered at high temperature was obtained. The prototypes produced are presented in Fig. 2. These prototypes were characterized using several techniques in order to determine their structural and textural properties and chemical composition.

The diffractograms obtained for the ceramic foam powders synthesized at 1200 °C are shown in Fig. 3. From the Tnternational Centre for Diffraction Data (ICDD) database, the presence of corundum, magnesium aluminum iron oxide and calcium aluminum silicate is observed. A refinement analysis showed that the chromium aluminum oxide phase (corundum type) represented 67.37%, followed by magnesium oxide (spinel type) with 19.12% and aluminosilicate with 13.51%, but this result would be taking into account only the phase adjustment by means

Fig. 2. Prototypes of ceramic foam filter supports synthesized from aluminum saline slags with several composite morphologies.

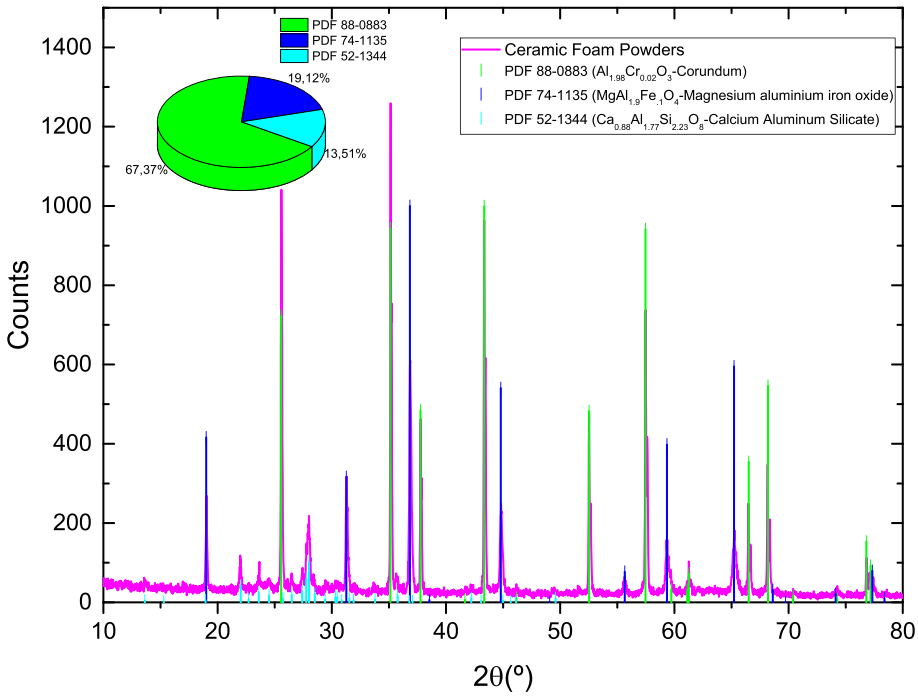

Fig. 3. Diffractogram of ceramic foam powders synthesized and calcined at 1200 °C. Corundum (#PDF 88–0883), magnesium aluminum iron oxide (#PDF 74–1135), calcium aluminum silicate (#PDF 52–1344) standards included.

of XRD. The chemical composition of these powders, which were obtained by mechanical shearing of the ceramic sponge filter, was determined by X-ray fluorescence (XRF) spectroscopy after the preparation of a borated glass bead by melting in an induction micro-furnace, mixing the Spectromelt A12 flux from Merck (Ref. 11,802) and the ground sample in approximate proportions of 20:1. The percentage of the main components of the samples by weight are included in **Table 1 (C)**, with the majority percentage corresponding to Al_2O_3 (75 wt%), followed by SiO_2 (8.2 wt%), MgO (4.64 wt%), Fe_2O_3 (4.15 wt%) and, finally, trace metals. These values are in partial accordance with the phases identified during the XRD analysis. The chemical composition found is not fully justified, but the phases detected are possible.

The curves obtained from the thermogravimetric and calorimetric analyses performed on the G/S mixture (0.7) using a temperature ramp of 40 °C/min are summarized in Fig. 4. The DSC curve shows various scenarios that occur in the heat flow associated with the transformations of glucose and clean saline slags. Thus, an endothermic peak (Fig. 4**-A**, red curve), possibly associated with the release of moisture and physisorbed species in the mixture, which are released spontaneously and generate this thermodynamic behavior, is observed at around 60 °C. In the same curve, two intensely negative peaks with T_{max} at 177 and 235 °C, which may be related to the caramelization of glucose and the subsequent transformation of caramel to carbon, are also identified. Several transition states corresponding to the decomposition (by combustion) of glucose and the transformations experienced by the saline slag powders, specifically related to the changes of state of alumina and other constituent oxides, are observed in the temperature range from 300 to 700 °C, whereas the degradation of inorganic materials and/or coal ash is seen between 1000 and 1400 °C.

As regards the mass loss with temperature, above 500 °C we identified several kinetic regimes associated with the transformations of glucose and structural changes in the saline slags (Fig. 4**-A**, blue curve). Initially we found that the loss of water, which occurred at between 50 and 100 °C, represented 1.31 wt%, followed by 15.2 wt% attributed to the glucose fusion process and subsequent caramelization. In the next range of transformations, there is another slope, with a weight decrease of 13 wt%, which we attribute to decomposition of the carbonaceous matrix generated. Finally, the remaining 5.8 wt% weight loss was due to the final stage of carbon removal by vaporization and structural transformations of the saline slag powders, which were mostly dominated by alumina transitions. The total sum of all the weight loss stages represented almost 45% of the original weight, thus meaning that the G/S mixture lost almost half its weight during the process and that the largest fraction was controlled by melting, caramelization, foaming, carbonization and decomposition of glucose.

The loss of mass with temperature, the conversion and the derivative of the conversion with respect to temperature are presented in Fig. 4**-B**, which confirms the previous comments regarding the mass evolution of the mixture. The curve for the first derivative of the conversion shows four peaks (according to the deconvoluted peaks) associated with the various conversion regimes of the mixture. The highest conversion/transformation is located between 238 and 290 °C, in which glucose monomers are transformed into porous carbon and swollen slag powders, as shown in **Fig. 1**–2c).

3.2. ZIF-8 characterization

The X-ray diffractograms obtained for both the synthesized MOF-ZIF8 and for the commercial one used in the comparison are included in Fig. 5. The type of structure identified in all samples corresponds to that of the ZIF-8 pattern, with a maximum intensity peak at a 2Θ value of 7.37°, followed by 10.38°, 12.77°, 18.07° and 16.52° in order of decreasing intensity. In the case of the commercial MOF, before and after impregnation on the foam at room temperature (Fig. 5, MA and MB), the structure remains unchanged and maintains the same crystallinity, with no alterations in the number of peaks present. In the case of the synthesis with methanol at room temperature (Fig. 5, MC), very low intensity peaks between the peaks corresponding to the basolite-like structure are observed, possibly due to another type of structure present in lower quantities or amorphous clusters of the crystals. The highest intensity peaks, which are narrow and very well defined, for the synthesized samples are found for the solvothermal synthesis method (Fig. 5, MD), which causes an accelerated growth of MOF crystals with large independent morphologies and an average crystallite size of 88.8

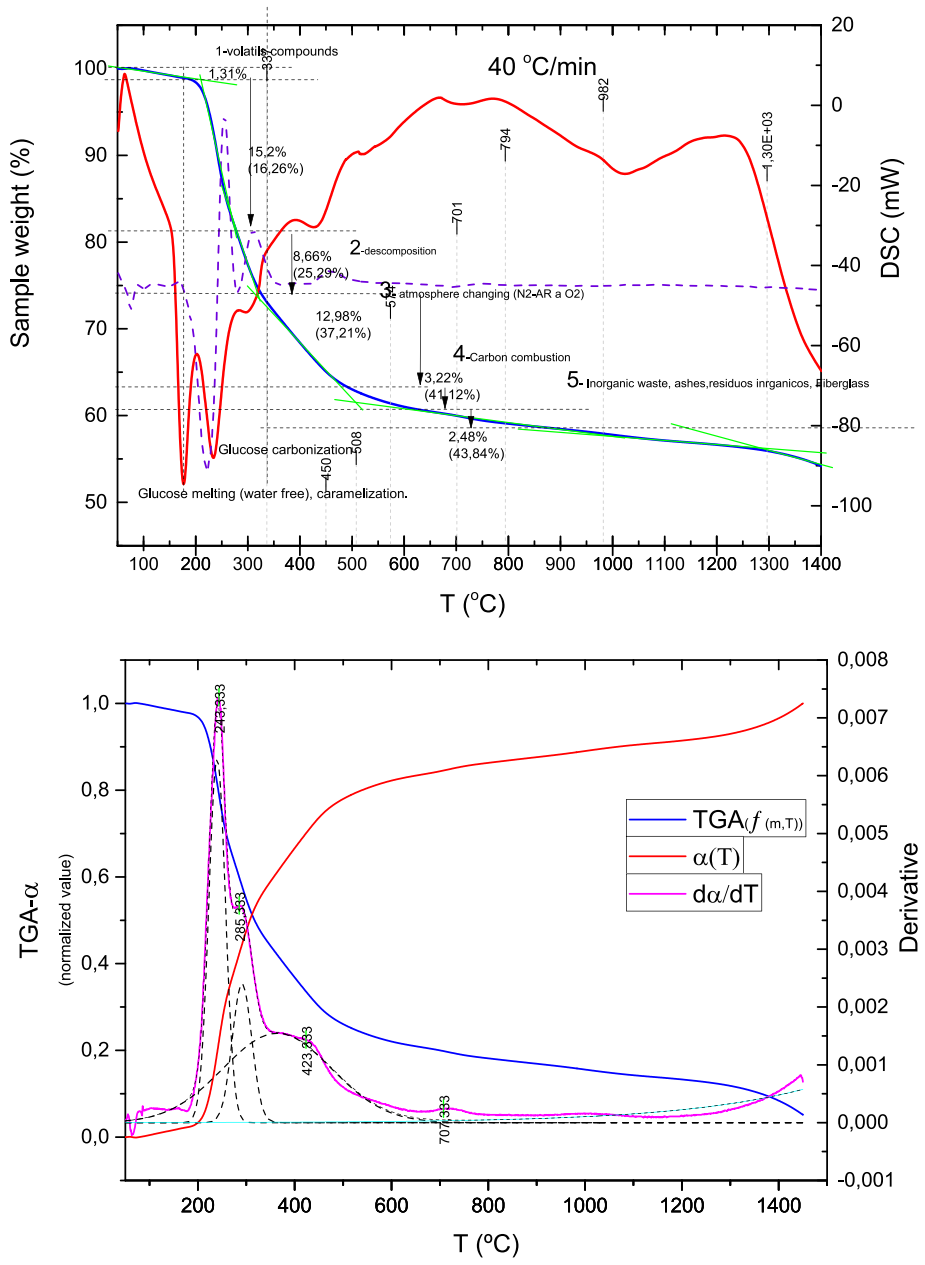

Fig. 4. (A) TGA-DSC analysis and (B) TGA-conversion and first derivative analysis for the G/S mixture (0.7) using a heating ramp of 40 °C/min up to a temperature of 1400 °C.

nm, which is larger than that for the MC sample (44.7 nm).

3.3. Characterization of the ceramic-MOF filter

Once the ceramic foam had been synthesized, the MOF powders obtained were impregnated on the ceramic foam support. The nitrogen adsorption isotherms for the MOF-ZIF-8 samples synthesized are shown in Fig. 6. The behavior of the isotherms in both the adsorption and desorption branches is very similar for both samples, with a single difference in the hysteresis loop stage. The adsorption isotherms are type I, which is related to microporous materials. MOF-1 presents a small increase and broadening of the loop that can be attributed to independent growth of the nanocrystals, low sintering and the generation of interconnected inkwell-type porosity. The textural properties of the three MOF samples (MOF-1, methanol synthesis; MOF-2, solvothermal method; and commercial ZIF-8 from Sigma-Aldrich) are presented in Table 2. For the synthesized samples, an increase of approximately 40% is seen for the sample synthesized following the methanol method. Reduction of S_{BET} for the solvothermal method may arise due to sintering of the nanocrystals during the heat treatment process. For the ceramic foam support, the S_{BET} was null or zero as a result of the final sintering temperature, which suggests that lower temperatures could result in a considerable improvement in the distribution, deposition and fixation of the MOF on the support. The textural properties of other commercial MOFs have also been included in Table 2 for comparison.

SEM images of a section of the ceramic-MOF-ZIF8 filter are shown in Figs. 7 and 1S, with the commercial ZIF-8 powders being deposited using the immersion procedure described above with methanol as dilution medium (see Section 2.4). Fig. 1S A) (left) shows SEM images for a cross-section of the ceramic foam filter. The morphology of the interstices formed during the foam expansion stage can easily be seen, along with large amorphous interconnected pores with an average area of 58 μm^2 uniformly distributed throughout the volume of the prototype (Fig. 7 A) and B) (left)). Similarly, Fig. 1S A) (center-right) clearly shows the

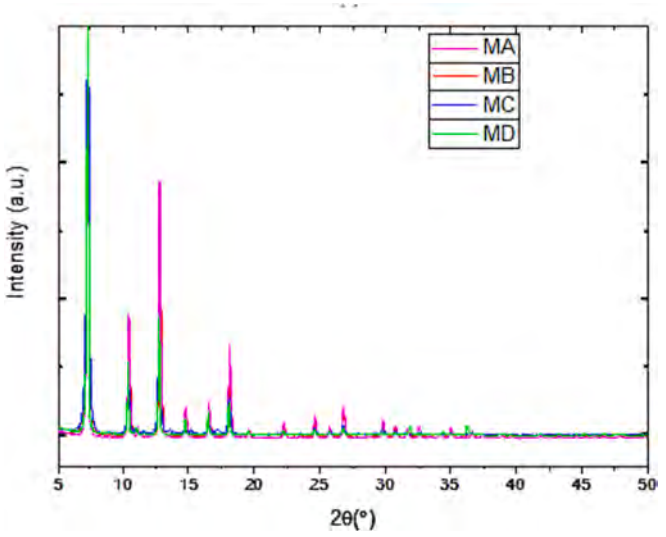

Fig. 5. Diffractograms of the MOF-ZIF8 powders synthesized by various methods. Commercial MA-MB ZIF-8 (before and after foam deposition, MA-MB, respectively), MOF-1 (MC), MOF-2 (MD).

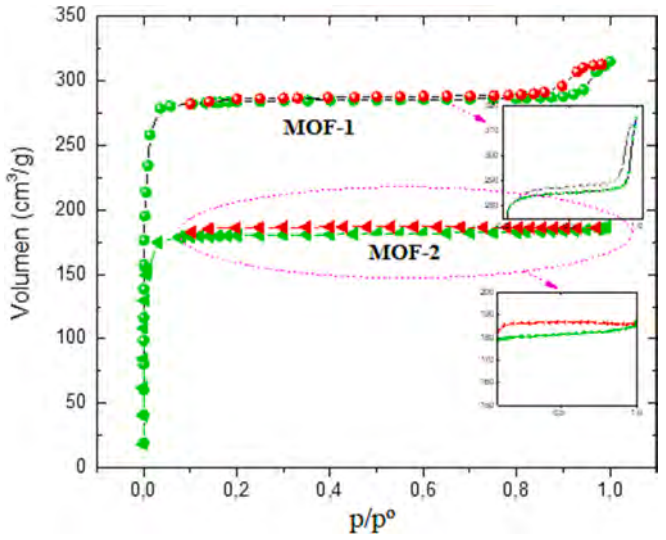

Fig. 6. N_2 adsorption-desorption isotherms for the MOF-ZIF8 powders synthesized.

Table 2
S_{BET} specific surface areas, pore volumes, volumes of CO_2 adsorbed and isosteric heats.

Sample	S_{BET} (m^2/g)	Vp (cm^3/g)	V_{CO2}* (mmol/g)	q_{st} (kJ/mol)
MOF-1	840	0.48	0.60**	18.59 (23.34)***
MOF-2	500	0.28	0.45**	18.91 (27.01)***
HKUST-1	1400	0.59	1.306	22.88 (24.94)***
MIL-53	465	1.05	1.029	22.06 (24.33)***
Fe-BTC	1000	0.52	0.621	21.05 (32.10)***
ZIF-8	1322	0.70	0.365	10.61 (13.05)***

Samples studied: MOF-1 (ZIF-8 synthesized at room-temperature), MOF-2 (ZIF-8 synthesized from a solvothermal method). Commercial MOFs: MIL-53 (Basolite A100), HKUST-1 or Cu-BTC (Basolite C300), Fe-BTC (Basolite F300) and ZIF-8 (Basolite Z1200).
(*) Volume of CO_2 adsorbed at 50 °C and 80 kPa.
(**) These data correspond to the ceramic-MOF filter.
(***) Isosteric heats at zero loading ($n = 0$).

presence of MOF particle deposits on the support surface. These are heterogeneously distributed, forming islands of MOF agglomerates as a result of the deposition method (saturated solution and immersion under agitation), which causes this effect in addition to a deficient coating due to very weak or almost null impregnation forces, thus resulting in the removal of the material deposited during washing. The distribution of irregular hexagonal plate-like particles of commercial ZIF-8, with an average particle size of 0.41 μm, can be seen in Fig. 7 A) and B) (right). The SEM images of the MOF-1 particles synthesized at room temperature in methanol and deposited on the ceramic foam are presented in Fig. 2S. **Fig. 2S** A) shows an amorphous MOF particle measuring 3.79 × 2.41 μm and representative of the entire batch. In the case of the ceramic foam pores, we observe two types of crater-type pores and smaller amorphous pores with average apparent diameters of 46 μm and average areas of 99 μm^2. The deposition and impregnation of the material on the ceramic surface presents the same deficiencies in terms of distribution and fixation of the MOF on the support described above, since this room-temperature method does not benefit these aspects, thus resulting in a weak film supported on the very easily removable ceramic, although with a better distribution compared to MOF-ceramic foam presented previously (see Fig. 7). However, it is still very poor in terms of optimal coating.

Fig. 8 presents a morphological analysis of the MOF particles deposited in situ on the ceramic-MOF-2 filter using the solvothermal method. In this case, the crystals grow directly on the surface of the ceramic foam (Fig. 8 A)-B)) and two important aspects are observed, namely a better deposition is achieved along with greater stabilization of the MOF particles, which evolve from the precursors to the final morphologies generated, adhering with greater cohesion forces as a result of the high pressure and temperature. **Figs. 8** and **3S** reveal that the distribution of the total mass of particles is not uniform over the entire ceramic volume but is located mainly in one region of the foam (Fig. 3S), with a small fraction in the rest of the volume (Fig. 8). This heterogeneous or localized distribution of MOF-2 could be improved by fixing the ceramic support inside the reactor during the solvothermal synthesis, which allows the porous body to be kept static during the entire reaction period and the total charge of particles that grow to be increased by complete immersion in the liquid matrix and by decreasing the turbulence during the solvothermal synthesis. Fig. 8 D)-E) shows large rhombic dodecahedron (RD) morphologies as the majority morphology, with a maximum size of 34 μm but an average size for the bulk particles of 11.51 μm (Fig. 3S). A small fraction also shows a perfectly defined truncated rhombic dodecahedron (TRD) morphology (Fig. 8 C)), with $\overline{dp}$ = 14.02 μm (two times smaller than RD), as well as the appearance of particles with interpenetrating twin RD particles. These morphological variants are the result of changes in the sequential ordering of the tetrahedral Hmim-Zn units due to the interference that the prototype could generate within the liquid matrix, favoring or disfavoring individual crystal growth and generating a mainly RD fraction, along with TRD, to a lesser extent, and a partial interpenetrating twin morphology (PIT).

The images obtained for MOF-1 and MOF-2, as well as the compositions obtained by EDX mapping in both cases, are summarized in **Figs. 9** and **4S**. Fig. 9 A)-B) shows the formation of grains of ZIF-8 and heterogeneous particles with various morphologies and sizes, including both large and very small particles with an RD or TRD morphology (Fig. 9 E)-F)), as observed in the fraction deposited on the ceramic support. This suggests that this morphological and topological effect is mainly due to cohesion and interaction forces during solvothermal synthesis and that other effects of growth and/or redispersion or diffusion resulting from the support are reduced. The composition obtained in this sample has the empirical formula $C_8H_{10}N_4Zn$, corresponding to the ZIF-8 frameworks (boxes in Fig. 9 E)-F)), with atomic percentages for C, N and Zn of 56.86% ± 0.98, 33.91% ± 1.07 and 7.68% ± 0.15, respectively ($C_{7.4}H_{10}N_{4.42}Zn$). In the case of the synthesis at room

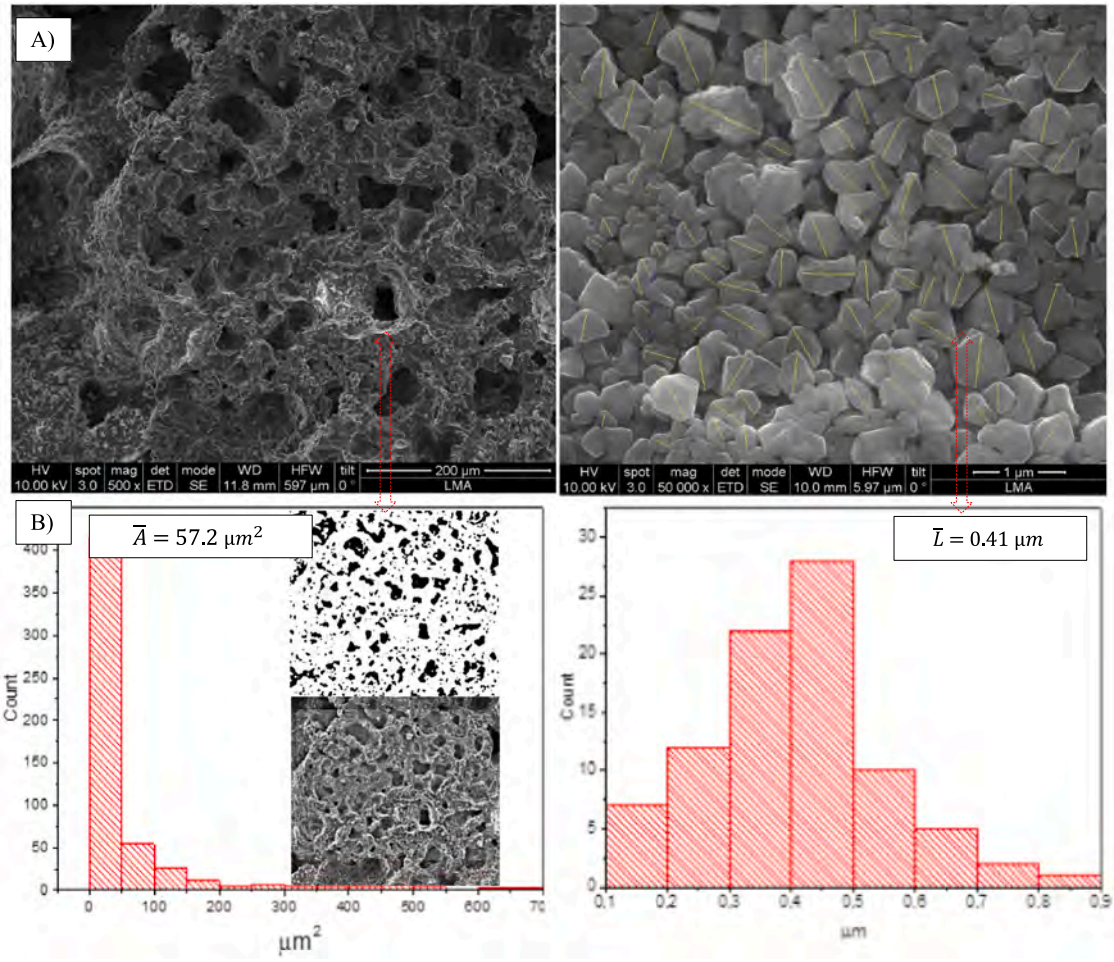

Fig. 7. (A) SEM images of the ceramic-MOF-ZIF8 filter and commercial MOF particles. (B) Pore-size distribution of the ceramic support (left) and particle-size distribution of ZIF-8 deposited on the ceramic support (right).

temperature in methanol, we observe much larger grains (Fig. 4S A)-B)) than those observed using the solvothermal method, and it becomes difficult to identify the size and morphology of the individual particles, thus indicating that they are below the detection level of the equipment. This could be attributed to the effect of redissolution and Otswal maturation of the MOF during sonication of the slurry [88], which results in regrouping of the crystals. These large agglomerates are formed from grouped crystalline structures, thus preventing their independent growth resulting in the aforementioned RD and TRD morphologies (Fig. 4S C)-D)) and generating open organometallic structures. The elemental composition analysis corroborates the presence of ZIF-8, with atomic % values for C, N and Zn of 53.96%, 37.68% and 5.96%, respectively. These results confirm the presence of MOF structures of the $C_8H_{10}N_4Zn$ type and is in agreement, in both cases, with the diffractograms presented in Fig. 5.

TEM images for MOF-1 and MOF-2 are shown in Fig. 10. The solvothermal method generated large crystals in the range 500–1500 nm. However, the irregular particles obtained from the methanol synthesis are due to agglomerates of independent nanocrystals with a sodalite-like structure (inset Fig. 10 B)-right) and a mean size of approximately 65 nm (Fig. 10 B-center). The size of the irregular agglomerates (Fig. 10 B-left)) is about 3000 nm. This difference between the growth of the crystals and the final morphologies of the particles discussed above appears to be associated with the intermolecular forces to which the precursors are subjected during the synthesis. Thus, in the case of the room-temperature method, the driving force that allows intimate contact of the precursors is the concentration gradient when working with excesses of both constituents, which results in very small nanocrystals that end up agglomerating. In contrast, when using the solvothermal method, the temperature (increase in the kinetic energy of the system, high frequencies of vibration of the atoms) and internal pressure (molecular confinement with an increase in intimate contact) used result in large uniform crystals that adopt specific positions, thus giving rise to well-defined morphologies (RD-TRD-PIT). This effect of different growth pathways impacts crystal size, morphology and topology as well as the textural and structural properties of both MOFs as a consequence of the synthesis method.

The TEM images for MOF-1 and MOF-2 included in **Figs. 11** and 5S correlate with the structural simulations carried out using the lattice parameters and interplanar distances obtained by image analysis, FFT and from the profile graphs. Fig. 11 A)-B)-C)-D) shows the surface patterns obtained in different regions that help us determine the interplanar distances and atomic distribution for each area selected by making fast Fourier and profile graphs. The surface pattern of diagonals, which presents an interplanar distance of 0.29 nm, is easily observable in Fig. 11 A). This distance is determined from the graphic profile (boxes Fig. 11 A) and complemented with the FFT pattern, with other interplanar distances (0.14, 0.19, 0.25, 0.28, 0.56 nm) being associated with the atomic distribution of ZIF-8. The complete pattern of the MOF network is observed in Fig. 11 C) (lower left box). The atomic distribution (FFT right box) is almost entirely consistent with the sodalite-like structure of the MOF and allows us to determine the interplanar distance for a large percentage of the atoms that form the structure using the interplanar distance values of 0.139, 0.142, 0.162, 0.170, 0.247, 0.282,

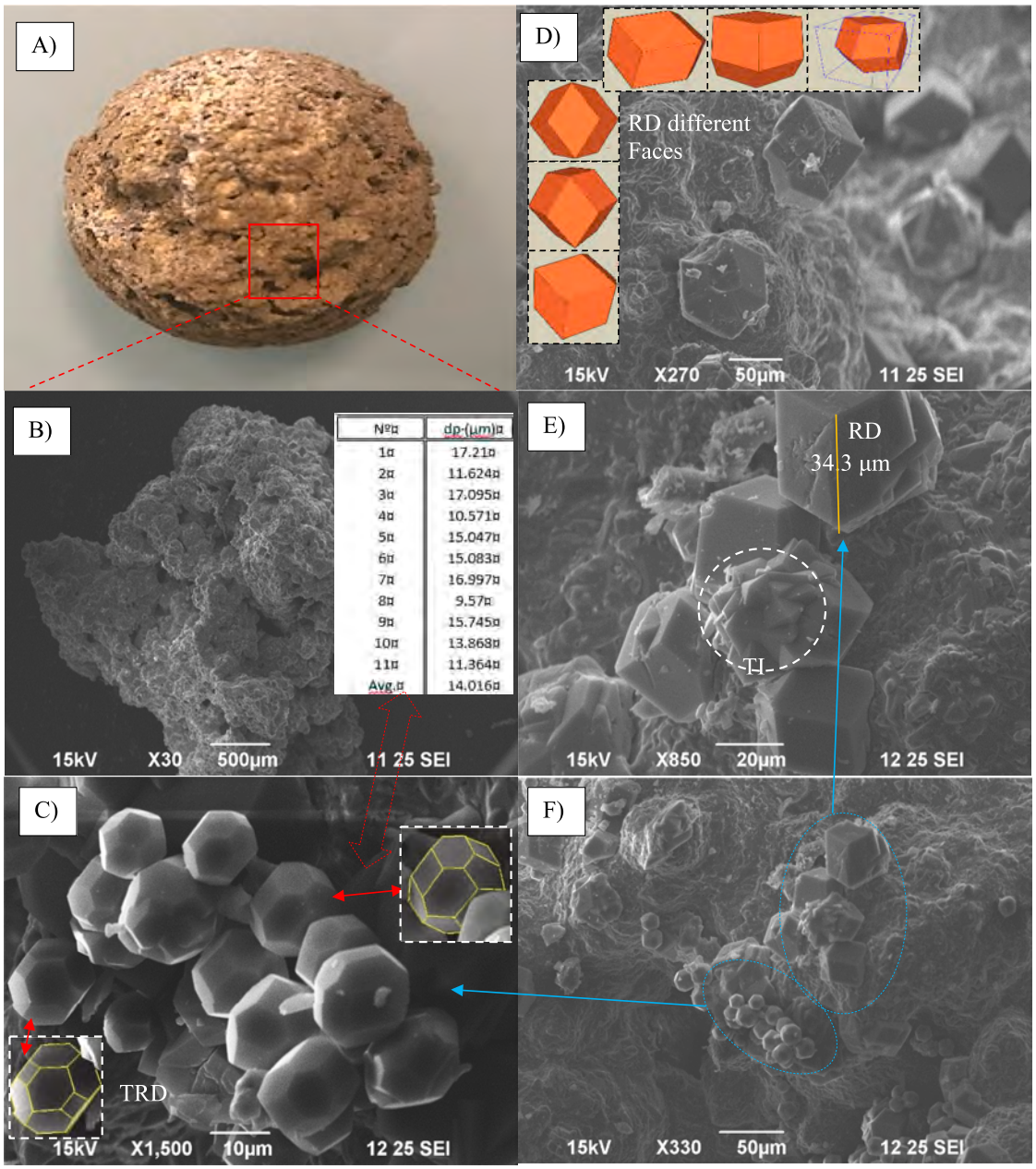

Fig. 8. SEM images of the ceramic-MOF-2 filter and MOF-2 particles grown on the support using the solvothermal method (region with light deposition). (A) Ceramic filter prototype, (B) ceramic support fraction, (C) MOF particles with zeolite-like morphology (truncated rhombic dodecahedron-TRD), (D)-(E) MOF particles with partial twin interpenetrated morphology-PIT and rhombohedral dodecahedron-RD, (F) combined MOF morphologies.

0.299, 0.450, 0.625 nm. It is also possible to identify similar patterns with distances of 0.691 (211), 0.565 (310), 0.513 (311), 0.265, 0.231, 0.182, and 0.132 nm for (FFT Fig. 11 B) and planes (200−210) in the patterns shown in Fig. 11 C)-FFT.

The TEM images for MOF-1 are shown in Fig. 5S. In all cases, the FFT patterns in said images appear as concentric rings that suggest the formation of amorphous structures. In this case, although the unit cell is the same (sodalite-like structure coinciding with the XRD pattern), the driving forces (concentration gradient, diffusion with low kinetic energy and low electrochemical gradient) are not sufficient to achieve the superposition of crystalline planes that allows particles with defined RD-TRD morphologies to be obtained. The crystals remain quasi-independent or form networks of few nuclei, which agglomerate randomly, thereby failing to form an ordered configuration such as that seen in Fig. 11 (MOF-2).

Using the data from the TEM images and from the diffractograms, Bragg's law can be used to determine the interplanar distances and the approximate planes corresponding to these interplanar distances. It is also possible to obtain the lattice parameters and the corresponding space groups from the experimental data. This information allows us to perform the structural simulations and model a ZIF-8. The values obtained for interplanar distances, Miller indices and corresponding planes from XRD, compared with the FFT analysis of the patterns in the TEM images, are summarized in Fig. 12. A composite image with the XRD pattern simulated from the calculated network parameters, using the experimental data, whose arrangement obeys the sodelite-type atomic distribution, as a unit cell are included in this figure. Here the values correspond to the interplanar distances associated with the position, of the diffraction angle 2 Θ, of each peak and therefore their respective planes and Miller indices, thus showing that the plane where the crystals grow preferentially is (110) with a 2Θ ≈ 7.3744° (d-interplanar ≈ 1.19844 nm, simulation and experimental). The superimposition of the

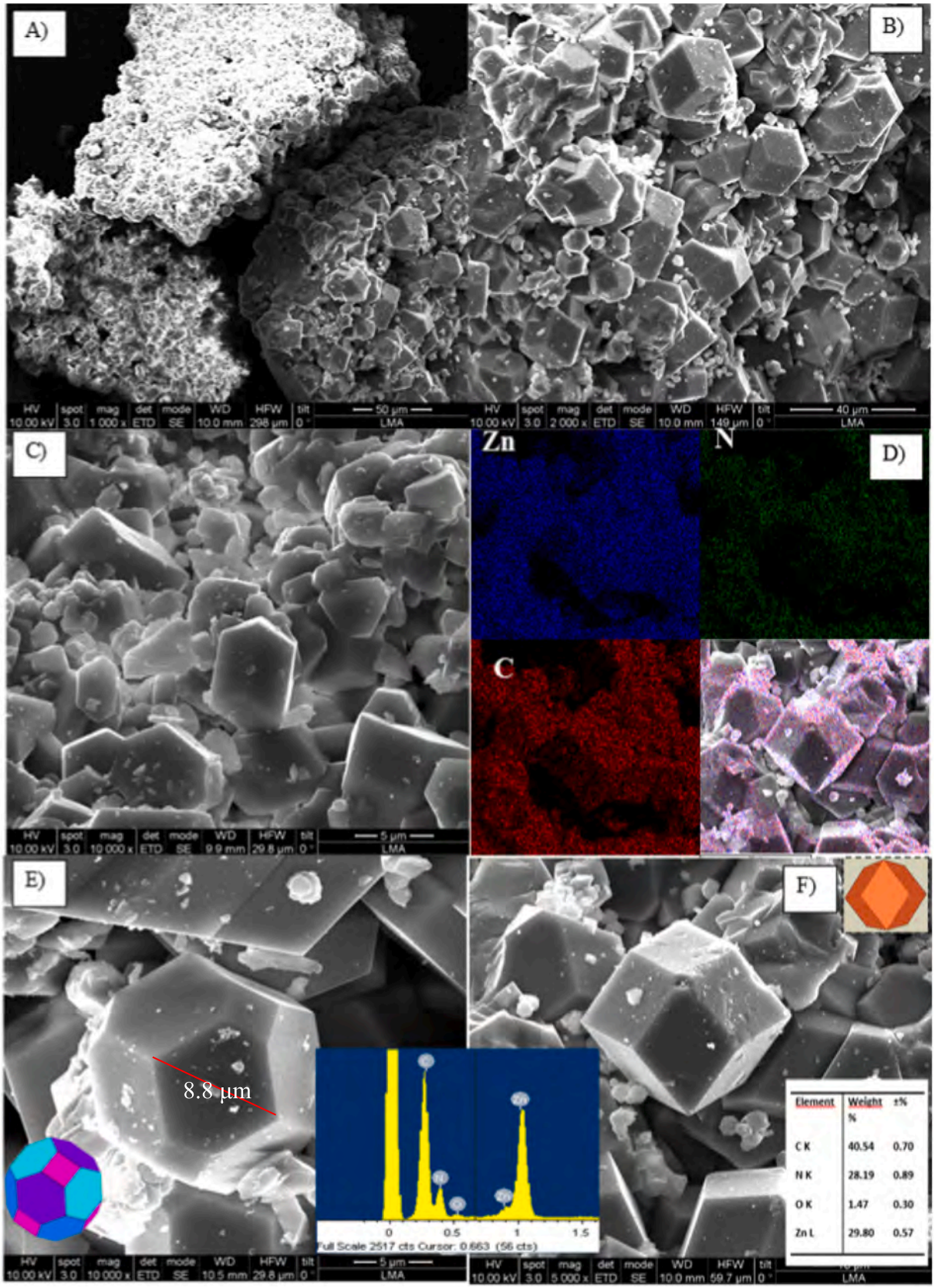

Fig. 9. SEM images of MOF-2 powders obtained by solvothermal synthesis. (A) Agglomerates of MOF particles form grains. (B)-(C) Images of the different morphologies and sizes of the MOF. (D)-(*E*)-(F) Elemental mapping of the MOF powders and EDX composition. (E)-(F) Morphology truncated rhombic dodecahedron and rhombic dodecahedron, respectively.

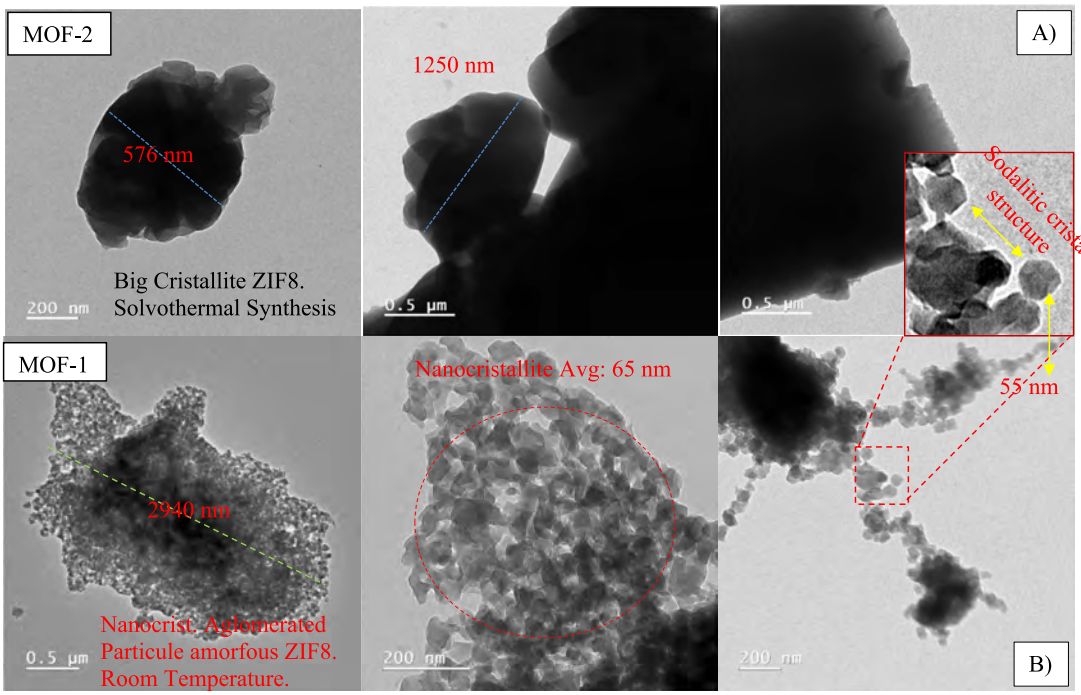

Fig. 10. TEM images of the MOF-2 and MOF-1 particles synthesized using the solvothermal and room-temperature methods. (A) Solvothermal synthesis (large crystallites 500–1500 nm). (B) Room-temperature synthesis (nanocrystallites 45–70 nm).

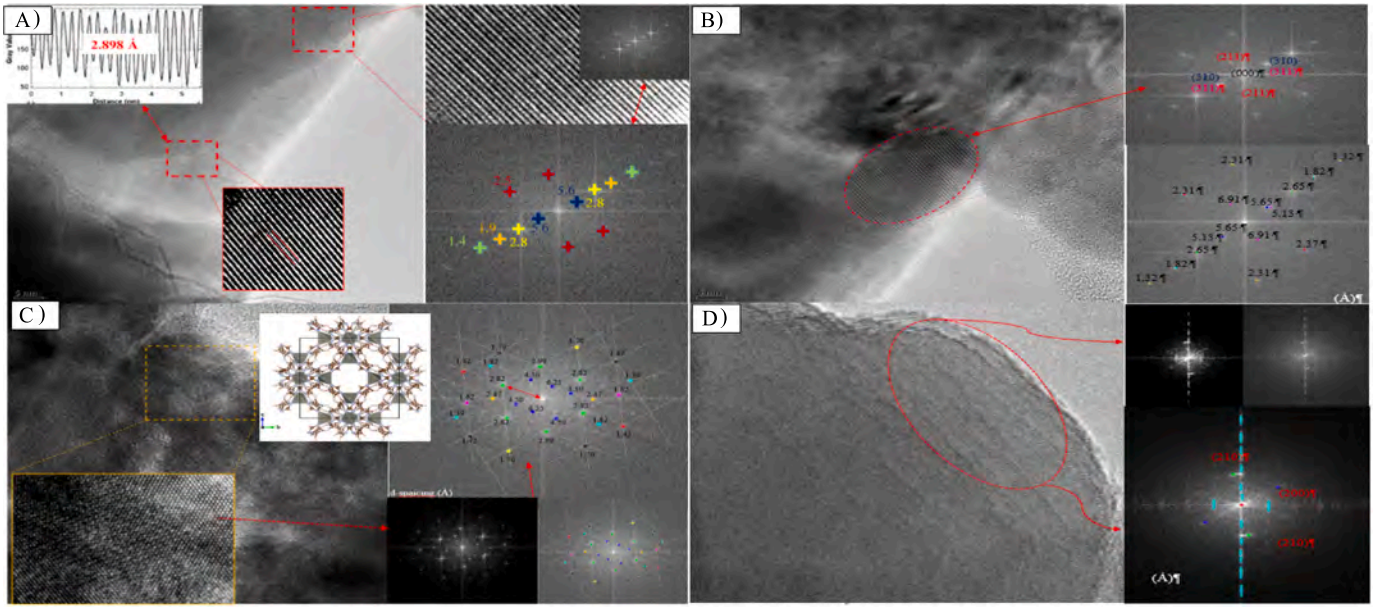

Fig. 11. Patterns and interplanar distances obtained from TEM images of MOF-2 applying FFT, profile graph and direct measurement, in different regions and mass fractions of the crystals.

ZIF-8 pattern, obtained by XRD for both MOFs, is also included (upper), on the simulated pattern with the tabulated data, indicating a 100% coincidence between both, which shows that both MOFs structurally obey the MOF ZIF-8 with sodalitic structure as unit cell.

3.4. CO_2 adsorption

The CO_2 adsorption capacity was determined for the ceramic-MOF filters at several temperatures in the range 50–300 °C. The experimental isotherms at corresponding temperatures of 50 and 200 °C are shown in Fig. 13; the maximum adsorption capacities for ceramic filters MOF-1 and MOF-2 at 50 °C and 80 kPa were 0.60 and 0.45 mmol/g, respectively. The behavior of the isotherms shows that the maximum amount adsorbed, as a function of the pressure gradient, decreases with an increase in temperature. The behavior observed for other commercial materials (HKUST-1, MIL-53, Fe-BTC and ZIF-8) is also included in these figures, with the highest CO_2 adsorption capacity corresponding to HKUST-1 (1.31 mmol/g). The amount adsorbed is included as mmol/$g_{ceramic\ filter+MOF}$ in the case of MOF-1 and MOF-2, and mmol/g_{MOF} in the case of the commercial MOF. However, the comparison must take into account that the amount of CO_2 adsorbed on the ceramic-MOF filter supports is negligible and that only 10 wt% MOF has been deposited.

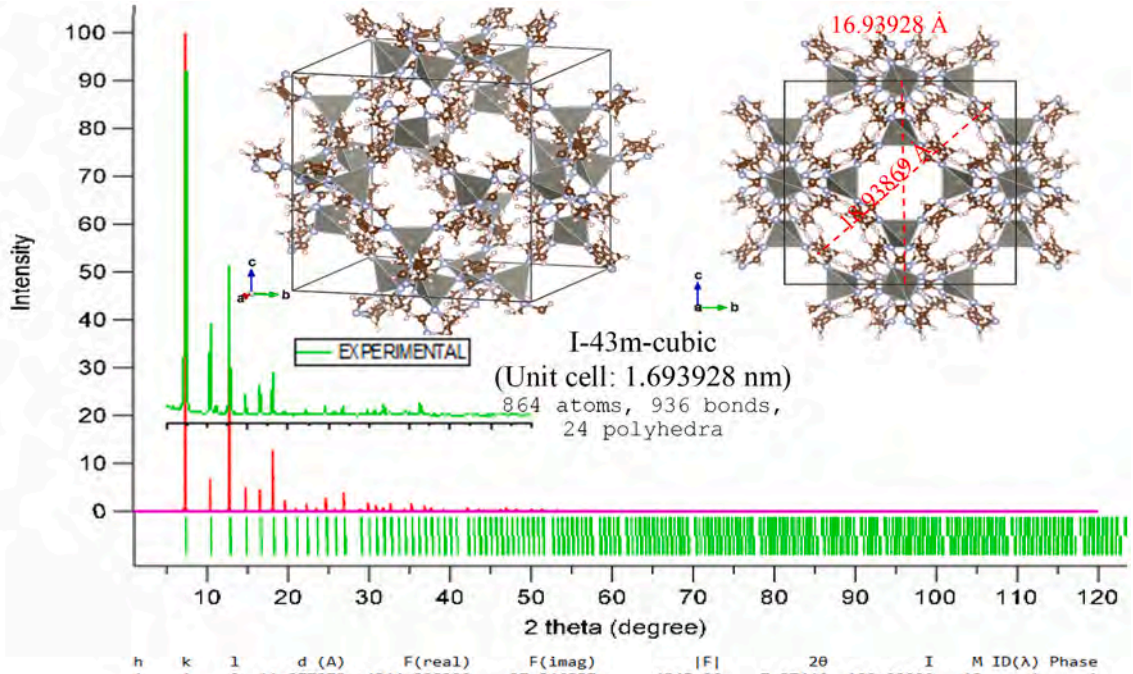

h	k	l	d (A)	F(real)	F(imag)	|F|	2θ	I	M	ID(λ)	Phase
1	1	0	11.977879	-4544.898220	-37.846557	4545.06	7.37446	100.00000	12	1	1
1	1	0	11.977879	-4545.485325	-38.002380	4545.64	7.39235	49.77008	12	2	1
2	0	0	8.469640	3476.605186	36.032326	3476.79	10.43629	14.53887	6	1	1
2	0	0	8.469640	3477.177897	36.179182	3477.37	10.46164	7.23631	6	2	1
2	1	1	6.915432	2638.418539	122.302175	2641.25	12.79067	11.11853	12	1	1
2	1	-1	6.915432	2639.129858	-50.955027	2639.62	12.79067	11.10482	12	1	1
2	1	1	6.915432	2638.986533	122.449970	2641.83	12.82178	5.53435	12	2	1
2	1	-1	6.915432	2639.701362	-50.812664	2640.19	12.82178	5.52750	12	2	1
2	2	0	5.988940	-1482.863297	-33.749441	1483.25	14.77969	2.61359	12	1	1
2	2	0	5.988940	-1483.417827	-33.885011	1483.8	14.81569	1.30131	12	2	1
3	1	0	5.356671	-1437.456387	-33.496354	1437.85	16.53575	3.90553	24	1	1
3	1	0	5.356671	-1438.009096	-33.630678	1438.4	16.57608	1.94455	24	2	1
2	2	2	4.889949	-4420.206089	-1323.031648	4613.96	18.12671	5.55138	4	1	1
2	2	-2	4.889949	-4429.097045	1124.316750	4569.57	18.12671	5.44508	4	1	1
2	2	2	4.889949	-4421.835243	-1323.462429	4615.65	18.17098	2.76382	4	2	1
2	2	-2	4.889949	-4430.770029	1123.952659	4571.1	18.17098	2.71073	4	2	1
3	2	-1	4.527213	517.233540	-397.386758	652.263	19.59285	0.56707	24	1	1
3	2	1	4.527213	514.452351	459.137155	689.542	19.59285	0.63375	24	1	1
3	2	-1	4.527213	517.773497	-397.275798	652.624	19.64078	0.28242	24	2	1
3	2	1	4.527213	514.978596	459.269004	690.022	19.64078	0.31572	24	2	1
4	0	0	4.234820	-290.906619	90.798315	304.747	20.96042	0.02691	6	1	1
4	0	0	4.234820	-289.323434	91.153446	303.343	21.01176	0.01327	6	2	1
4	1	-1	3.992626	614.419022	1297.762040	1435.86	22.24762	1.05568	12	1	1
4	1	1	3.992626	619.860369	-1353.334411	1488.54	22.24762	1.13456	12	1	1
3	3	0	3.992626	612.597797	-27.087729	613.196	22.24762	0.19253	12	1	1
4	1	-1	3.992626	613.895782	1297.677248	1435.56	22.30219	0.52494	12	2	1
4	1	1	3.992626	619.364012	-1353.461961	1488.45	22.30219	0.56432	12	2	1
3	3	0	3.992626	612.092034	-27.190492	612.696	22.30219	0.09562	12	2	1
4	2	0	3.787738	489.679980	30.677147	490.64	23.46770	0.22053	24	1	1
4	2	0	3.787738	490.212370	30.797597	491.179	23.52535	0.10994	24	2	1
3	3	2	3.611467	2157.490314	178.479086	2164.86	24.63067	1.93970	12	1	1
3	3	-2	3.611467	2159.718242	-109.000100	2162.47	24.63067	1.93541	12	1	1
3	3	2	3.611467	2158.048313	178.626899	2165.43	24.69126	0.96536	12	2	1
3	3	-2	3.611467	2160.287165	-108.866924	2163.03	24.69126	0.96323	12	2	1
4	2	2	3.457716	-1152.639891	1440.001179	1844.5	25.74428	1.28296	12	1	1
4	2	-2	3.457716	-1149.669806	-1503.916369	1893.01	25.74428	1.35133	12	1	1
4	2	2	3.457716	-1153.189826	1439.888978	1844.76	25.80770	0.63834	12	2	1
4	2	-2	3.457716	-1150.204896	-1504.057722	1893.45	25.80770	0.67248	12	2	1
4	3	-1	3.322066	-1889.145262	1176.933606	2225.77	26.81470	3.42814	24	1	1
4	3	1	3.322066	-1883.862933	-1245.691031	2258.47	26.81470	3.52962	24	1	1
5	1	0	3.322066	-373.622215	-31.379958	374.938	26.81470	0.09728	24	1	1
4	3	-1	3.322066	-1889.718425	1176.815452	2226.19	26.88086	1.70580	24	2	1
4	3	1	3.322066	-1884.410011	-1245.850273	2259.01	26.88086	1.75647	24	2	1
5	1	0	3.322066	-374.158623	-31.503836	375.483	26.88086	0.04853	24	2	1
5	2	-1	3.092675	651.280283	-498.412766	820.111	28.84512	0.39854	24	1	1
5	2	1	3.092675	647.736609	559.776905	856.103	28.84512	0.43429	24	1	1
5	2	-1	3.092675	651.821347	-498.304694	820.475	28.91650	0.19840	24	2	1
5	2	1	3.092675	648.260254	559.909777	856.586	28.91650	0.21625	24	2	1
4	4	0	2.994470	4072.531967	97.279616	4073.69	29.81267	4.58190	12	1	1
4	4	0	2.994470	4074.171831	97.666937	4075.34	29.88656	2.28068	12	2	1

Fig. 12. XRD pattern simulated with the structural parameters of MOF-2 (a = 1.69389 nm) (upper). Bottom, miller indices, interplanar distances, peak intensities and phase, determined by simulations.

The ceramic filter has several properties that justify the deposit of MOF on its surface. It provides mechanical and thermal resistance to the MOF, and therefore to its application. In the same way, it allows the MOF particles to be dispersed, giving a greater CO_2 adsorption capacity. In the present work, the adsorption of CO_2 has been studied up to 300 °C, a temperature value that is not too high where the MOFs studied are resistant. The dispersion of the MOF in the ceramic material has allowed them to have, for the amount of MOF evaluated, a greater adsorption capacity than if the pure MOF is considered. Therefore, the presence of the ceramic filter is a clear advantage.

The isosteric heat of adsorption allows to describe the heat effects produced during the adsorption of a gas, as in this case CO_2. Isosteric

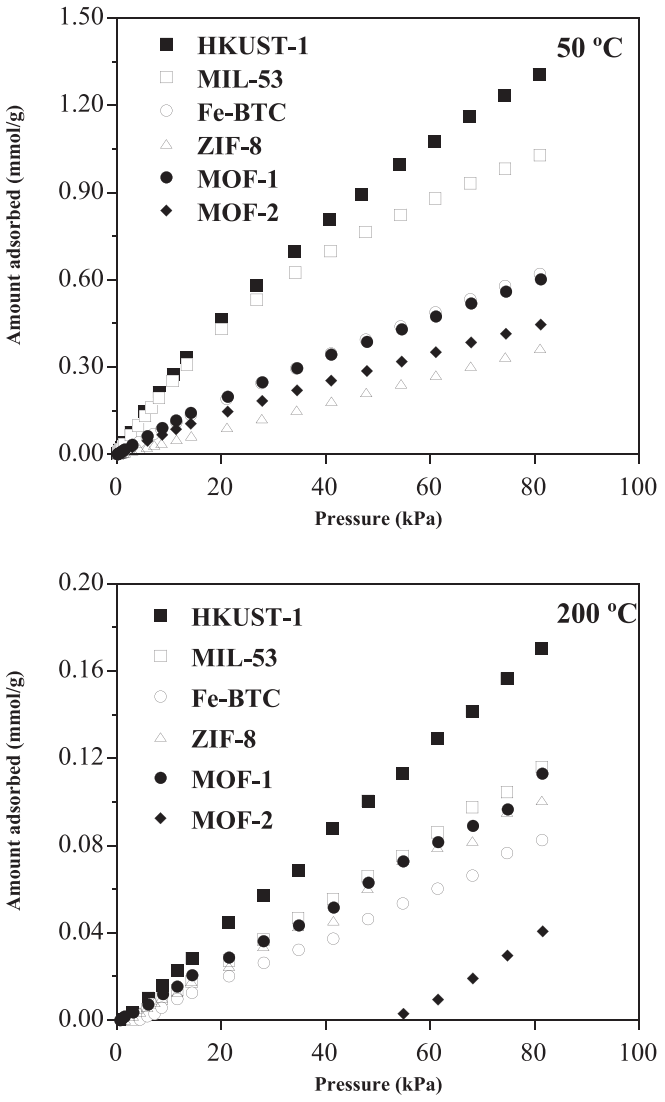

Fig. 13. CO_2 adsorption isotherm at 50 and 200 °C for ceramic-MOF filters (MOF-1 and MOF-2). Commercial MOFs are also included for comparison. The amount adsorbed is included as mmol/$g_{ceramic+MOF}$ in the case of MOF-1 and MOF-2, and mmol/g_{MOF} in the case of the commercial MOF.

heat defines the energy change resulting from the phase change of an infinitesimal number of molecules at constant pressure and temperature and a specific charge of adsorbate. The Clausius-Clapeyron equation allows to calculate the isosteric heat of adsorption [89], which relates the isosteric heat to the change in pressure of the bulk gas phase as a consequence of a change in temperature for a constant amount of adsorbed gas. The equation can be written as:

$$q_{st} = -R\left[\frac{\partial lnp}{\partial(1/T)}\right]_n \quad (1)$$

where p (kPa) is the equilibrium pressure, n is the amount of gas adsorbed at temperature T (K) and R (kJ/mol·K) is the universal gas constant. Initially it is necessary to determine the CO_2 adsorption capacity with pressure (adsorption isotherms) at various temperatures (experimental results indicated above and presented in Fig. 13 for two temperatures). Next, make a representation of ln*(n)* versus *1/T*, named as isosteres. The slope of each of these linear representations provides a value of the isosteric heat (q_{st}) that it can represent as a function of the amount adsorbed (n). In this case, the evolution is included in Fig. 14. The results show that the isosteric heats are constant with loading, in some cases increasing at low loading. These values suggest that the adsorption process needs a small amount of energy to be activated and, therefore, that regeneration of the material also needs only a small amount of energy, thus meaning that it is easy to regenerate. As the relationship between the isosteric heat and loading is essentially linear, some authors have related it to the surface energy homogeneity of the materials. The difference in values between the materials (see Table 2) must be related to the surface chemical composition, thus suggesting that the presence of Zn (ZIF-8) reduces the surface–CO_2 interaction, confirming this when it comes to commercial ZIF-8 given which presents a lower isosteric heat than the other materials. The values observed with respect to zero coating ($n = 0$) increase slightly. This result may be due to the fact that the surface is clean and the interaction with the first CO_2 molecules adsorbed increases.

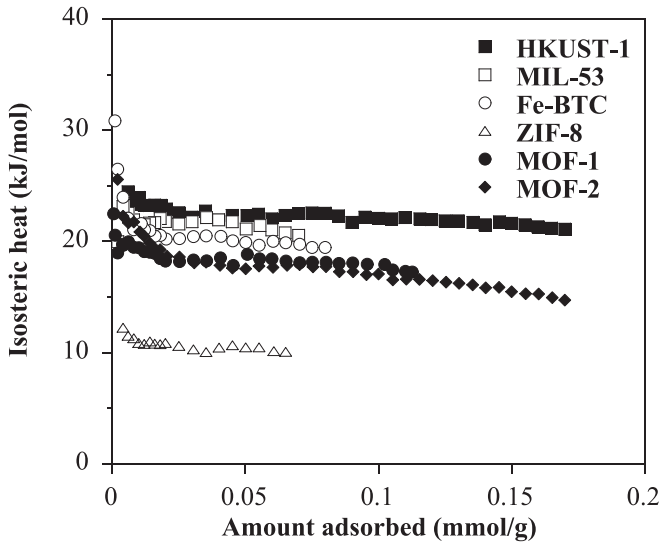

Fig. 14. Isosteric heat of CO_2 adsorption as a function of the amount of CO_2 adsorbed on the MOF.

4. Summary and conclusions

This work has presented the synthesis of ceramic-MOF filters from aluminum saline slags for the removal of CO_2. These slags are used as the main raw material for production of the ceramic support using a foam and porosity-generation method based on the use of glucose as a foaming polymer and generator of a carbon template. The effect of temperature and reaction time on the porosity of the ceramic foam was verified during the glucose foaming and carbonization stages. Similarly, two methods for the synthesis of ZIF-8 were evaluated, followed by deposition on the ceramic support. The synthesis of ZIF-8 at room temperature in methanol resulted in a material with a specific surface area of 800 m^2/g with independent sodalite crystals, whereas the solvothermal synthesis gave a specific surface area of 500 m^2/g and slightly lower thermal stability. The surface distribution and deposition of the MOF on the support was also affected by the synthesis method, with a better adherence being observed when using the solvothermal method.

The performance of the ceramic-MOF filters (MOF-1 and MOF-2) as CO_2 adsorbents was evaluated, in both cases finding similar adsorption capacities and isoteric heats of adsorption. These results are indicative of the adsorption capacity and ease of regeneration for both MOF filters, although with differences due to their topologies and surface properties.

The results presented in this work indicate that aluminum saline slags can be used as a starting material for the synthesis of ceramic filters and that they can be used as MOF supports that allow the storage of greenhouse gases such as CO_2.

Author contributions

All the authors conceived, designed, and performed the experiments, analyzed the data, and drafted the manuscript.

Declaration of Competing Interest

The authors declare that they have no known competing financial interests or personal relationships that could have appeared to influence the work reported in this paper.

Data availability

No data was used for the research described in the article.

Acknowledgements

The authors are grateful for financial support from the Spanish Ministry of Science and Innovation (AEI/MINECO) and Gouvernment of Navarra through projects PID2020-112656RB-C21 and 0011-3673-2021-000004. JJTH thanks Universidad Pública de Navarra for a post-doctoral grant.

Appendix A. Supplementary data

Supplementary data to this article can be found online at https://doi.org/10.1016/j.powtec.2023.118962.

References

[1] M. Van der Hoeven, CO_2 Emissions from Fuel Combustion–Highlights, IEA Stat, 2011.
[2] S.-Y. Lee, S.-J. Park, A review on solid adsorbents for carbon dioxide capture, J. Ind. Eng. Chem. 23 (2015) 1–11, https://doi.org/10.1016/j.jiec.2014.09.001.
[3] A. Stangeland, A model for the CO_2 capture potential, Int. J. Greenh. Gas Control. 1 (2007) 418–429.
[4] J. Garrett, S. McCoy, 4th IEA International CCS Regulatory Network Meeting, 2012.
[5] J.C. Minx, W.F. Lamb, M.W. Callaghan, S. Fuss, J. Hilaire, F. Creutzig, T. Amann, T. Beringer, W. de Oliveira Garcia, J. Hartmann, T. Khanna, D. Lenzi, G. Luderer, G. F. Nemet, J. Rogelj, P. Smith, J.L. Vicente Vicente, J. Wilcox, M. del Mar Zamora Dominguez, Negative emissions—part 1: research landscape and synthesis, Environ. Res. Lett. 13 (2018) 63001, https://doi.org/10.1088/1748-9326/aabf9b.
[6] I.E. Agency, CO_2 Emissions from Fuel Combustion 2014, 2014, https://doi.org/10.1787/co2_fuel-2014-en.
[7] C. Le Quéré, R.M. Andrew, P. Friedlingstein, S. Sitch, J. Hauck, J. Pongratz, P. A. Pickers, J.I. Korsbakken, G.P. Peters, J.G. Canadell, A. Arneth, V.K. Arora, L. Barbero, A. Bastos, L. Bopp, F. Chevallier, L.P. Chini, P. Ciais, S.C. Doney, T. Gkritzalis, D.S. Goll, I. Harris, V. Haverd, F.M. Hoffman, M. Hoppema, R. A. Houghton, G. Hurtt, T. Ilyina, A.K. Jain, T. Johannessen, C.D. Jones, E. Kato, R. F. Keeling, K.K. Goldewijk, P. Landschützer, N. Lefèvre, S. Lienert, Z. Liu, D. Lombardozzi, N. Metzl, D.R. Munro, J.E.M.S. Nabel, S. Nakaoka, C. Neill, A. Olsen, T. Ono, P. Patra, A. Peregon, W. Peters, P. Peylin, B. Pfeil, D. Pierrot, B. Poulter, G. Rehder, L. Resplandy, E. Robertson, M. Rocher, C. Rödenbeck, U. Schuster, J. Schwinger, R. Séférian, I. Skjelvan, T. Steinhoff, A. Sutton, P.P. Tans, H. Tian, B. Tilbrook, F.N. Tubiello, I.T. van der Laan-Luijkx, G.R. van der Werf, N. Viovy, A.P. Walker, A.J. Wiltshire, R. Wright, S. Zaehle, B. Zheng, Global carbon budget 2018, Earth Syst. Sci. Data. 10 (2018) 2141–2194, https://doi.org/10.5194/essd-10-2141-2018.
[8] M. Yang, C. Ma, M. Xu, S. Wang, L. Xu, Recent advances in CO_2 adsorption from air: a review, Curr. Pollut. Rep. 5 (2019) 272–293, https://doi.org/10.1007/s40726-019-00128-1.
[9] Y. Belmabkhout, V. Guillerm, M. Eddaoudi, Low concentration CO_2 capture using physical adsorbents: are metal–organic frameworks becoming the new benchmark materials, Chem. Eng. J. 296 (2016) 386–397, https://doi.org/10.1016/j.cej.2016.03.124.
[10] P. Nugent, Y. Belmabkhout, S.D. Burd, A.J. Cairns, R. Luebke, K. Forrest, T. Pham, S. Ma, B. Space, L. Wojtas, M. Eddaoudi, M.J. Zaworotko, Porous materials with optimal adsorption thermodynamics and kinetics for CO_2 separation, Nature. 495 (2013) 80–84, https://doi.org/10.1038/nature11893.
[11] P.M. Bhatt, Y. Belmabkhout, A. Cadiau, K. Adil, O. Shekhah, A. Shkurenko, L. J. Barbour, M. Eddaoudi, A fine-tuned fluorinated MOF addresses the needs for trace CO_2 removal and air capture using physisorption, J. Am. Chem. Soc. 138 (2016) 9301–9307, https://doi.org/10.1021/jacs.6b05345.
[12] A. Gil, L. Santamaría, S.A. Korili, M.A. Vicente, L.V. Barbosa, S.D. de Souza, L. Marçal, E.H. de Faria, K.J. Ciuffi, A review of organic-inorganic hybrid clay based adsorbents for contaminants removal: synthesis, perspectives and applications, J. Environ. Chem. Eng. 9 (2021), 105808, https://doi.org/10.1016/j.jece.2021.105808.
[13] L. Santamaria, S.A. Korili, A. Gil, Layered double hydroxides for CO_2 adsorption at moderate temperatures: synthesis and amelioration strategies, Chem. Eng. J. 455 (2023), 140551, https://doi.org/10.1016/j.cej.2022.140551.
[14] A.R. Millward, O.M. Yaghi, Metal−organic frameworks with exceptionally high capacity for storage of carbon dioxide at room temperature, J. Am. Chem. Soc. 127 (2005) 17998–17999, https://doi.org/10.1021/ja0570032.
[15] C.A. Trickett, A. Helal, B.A. Al-Maythalony, Z.H. Yamani, K.E. Cordova, O. M. Yaghi, The chemistry of metal-organic frameworks for CO_2 capture, regeneration and conversion, Nat. Rev. Mater. 2 (2017) 1–16, https://doi.org/10.1038/natrevmats.2017.45.
[16] R. Freund, O. Zaremba, G. Arnauts, R. Ameloot, G. Skorupskii, M. Dincă, A. Bavykina, J. Gascon, A. Ejsmont, J. Goscianska, M. Kalmutzki, U. Lächelt, E. Ploetz, C.S. Diercks, S. Wuttke, The current status of MOF and COF applications, Angew. Chem. Int. Ed. 60 (2021) 23975–24001, https://doi.org/10.1002/anie.202106259.
[17] J. Lee, O.K. Farha, J. Roberts, K.A. Scheidt, S.T. Nguyen, J.T. Hupp, Metal-organic framework materials as catalysts, Chem. Soc. Rev. 38 (2009) 1450–1459, https://doi.org/10.1039/b807080f.
[18] K.S. Park, Z. Ni, A.P. Côté, J.Y. Choi, R. Huang, F.J. Uribe-Romo, H.K. Chae, M. O'Keeffe, O.M. Yaghi, Exceptional chemical and thermal stability of zeolitic imidazolate frameworks, Proc. Natl. Acad. Sci. U. S. A. 103 (2006) 10186–10191, https://doi.org/10.1073/pnas.0602439103.
[19] B. Chen, Z. Yang, Y. Zhu, Y. Xia, Zeolitic imidazolate framework materials: recent progress in synthesis and applications, J. Mater. Chem. A 2 (2014) 16811–16831, https://doi.org/10.1039/c4ta02984d.
[20] Y. Hu, H. Kazemian, S. Rohani, Y. Huang, Y. Song, In situ high pressure study of ZIF-8 by FTIR spectroscopy, Chem. Commun. 47 (2011) 12694–12696, https://doi.org/10.1039/C1CC15525C.
[21] O. Kolmykov, J.M. Commenge, H. Alem, E. Girot, K. Mozet, G. Medjahdi, R. Schneider, Microfluidic reactors for the size-controlled synthesis of ZIF-8 crystals in aqueous phase, Mater. Des. 122 (2017) 31–41, https://doi.org/10.1016/j.matdes.2017.03.002.
[22] J. Wang, L. Yao, E. Hu, Y. Cui, D. Yang, G. Qian, MnO_2 decorated ZIF-8@GOx for synergistic chemodynamic and starvation therapy of cancer, J. Solid State Chem. 298 (2021), 122102, https://doi.org/10.1016/j.jssc.2021.122102.
[23] V. Hoseinpour, Z. Shariatinia, Applications of zeolitic imidazolate framework-8 (ZIF-8) in bone tissue engineering: a review, Tissue Cell 72 (2021), 101588, https://doi.org/10.1016/j.tice.2021.101588.
[24] B. Rahul, P. Anh, W. Bo, K. Carolyn, F. Hiroyasu, O. Michael, Y.O. M, High-throughput synthesis of zeolitic imidazolate frameworks and application to CO_2 capture, Science 319 (2008) 939–943, https://doi.org/10.1126/science.1152516.
[25] M. Bergaoui, M. Khalfaoui, A. Awadallah-F, S. Al-Muhtaseb, A review of the features and applications of ZIF-8 and its derivatives for separating CO_2 and isomers of C_3- and C_4- hydrocarbons, J. Nat. Gas Sci. Eng. 96 (2021), 104289, https://doi.org/10.1016/j.jngse.2021.104289.
[26] J.-H. Park, S.-H. Park, S.-H. Jhung, Microwave-syntheses of zeolitic imidazolate framework material, ZIF-8, J. Korean Chem. Soc. 53 (2009) 553–559.
[27] G. Lu, S. Li, Z. Guo, O.K. Farha, B.G. Hauser, X. Qi, Y. Wang, X. Wang, S. Han, X. Liu, J.S. DuChene, H. Zhang, Q. Zhang, X. Chen, J. Ma, S.C.J. Loo, W.D. Wei, Y. Yang, J.T. Hupp, F. Huo, Imparting functionality to a metal–organic framework material by controlled nanoparticle encapsulation, Nat. Chem. 4 (2012) 310–316, https://doi.org/10.1038/nchem.1272.
[28] M. Faustini, J. Kim, G.-Y. Jeong, J.Y. Kim, H.R. Moon, W.-S. Ahn, D.-P. Kim, Microfluidic approach toward continuous and ultrafast synthesis of metal–organic framework crystals and hetero structures in confined microdroplets, J. Am. Chem. Soc. 135 (2013) 14619–14626.
[29] Y. Pan, Y. Liu, G. Zeng, L. Zhao, Z. Lai, Rapid synthesis of zeolitic imidazolate framework-8 (ZIF-8) nanocrystals in an aqueous system, Chem. Commun. 47 (2011) 2071–2073, https://doi.org/10.1039/c0cc05002d.
[30] J. Xie, N. Yan, F. Liu, Z. Qu, S. Yang, P. Liu, CO_2 adsorption performance of ZIF-7 and its endurance in flue gas components, Front. Environ. Sci. Eng. 8 (2014) 162–168, https://doi.org/10.1007/s11783-013-0507-2.
[31] J. Lucero, C. Osuna, J.M. Crawford, M.A. Carreon, Microwave-assisted synthesis of porous organic cages CC3 and CC2, CrystEngComm. 21 (2019) 4534–4537, https://doi.org/10.1039/C9CE00880B.
[32] A. Martinez Joaristi, J. Juan-Alcañiz, P. Serra-Crespo, F. Kapteijn, J. Gascon, Electrochemical synthesis of some archetypical Zn^{2+}, Cu^{2+}, and Al^{3+} metal organic frameworks, Cryst. Growth Des. 12 (2012) 3489–3498, https://doi.org/10.1021/cg300552w.
[33] B.P. Biswal, D.B. Shinde, V.K. Pillai, R. Banerjee, Stabilization of graphene quantum dots (GQDs) by encapsulation inside zeolitic imidazolate framework nanocrystals for photoluminescence tuning, Nanoscale. 5 (2013) 10556–10561.
[34] Q. Shi, Z. Chen, Z. Song, J. Li, J. Dong, Synthesis of ZIF-8 and ZIF-67 by steam-assisted conversion and an investigation of their tribological behaviors, Angew. Chem. 123 (2011) 698–701.
[35] H.-Y. Cho, J. Kim, S.-N. Kim, W.-S. Ahn, High yield 1-L scale synthesis of ZIF-8 via a sonochemical route, Microporous Mesoporous Mater. 169 (2013) 180–184.
[36] F. Fu, B. Zheng, L.-H. Xie, H. Du, S. Du, Z. Dong, Size-controllable synthesis of zeolitic imidazolate framework/carbon nanotube composites, Crystals. 8 (2018) 367.
[37] A. Awadallah-F, F. Hillman, S.A. Al-Muhtaseb, H.-K. Jeong, On the nanogate-opening pressures of copper-doped zeolitic imidazolate framework ZIF-8 for the adsorption of propane, propylene, isobutane, and n-butane, J. Mater. Sci. 54 (2019) 5513–5527, https://doi.org/10.1007/s10853-018-03249-y.

[38] G. Huang, D.M. Yin, L.M. Wang, A general strategy for coating metal-organic frameworks on diverse components and architectures, J. Mater. Chem. A 4 (2016) 15106–15116, https://doi.org/10.1039/c6ta05389k.

[39] A. Gil, Management of the salt cake from secondary aluminum fusion processes, Ind. Eng. Chem. Res. 44 (2005) 8852–8857, https://doi.org/10.1021/ie050835o.

[40] A. Gil, S. Albeniz, S.A. Korili, Valorization of the saline slags generated during secondary aluminium melting processes as adsorbents for the removal of heavy metal ions from aqueous solutions, Chem. Eng. J. 251 (2014) 43–50, https://doi.org/10.1016/j.cej.2014.04.056.

[41] N. Ünlü, M.G. Drouet, Comparison of salt-free aluminum dross treatment processes, Resour. Conserv. Recycl. 36 (2002) 61–72.

[42] M. Sarker, S. Rahman, M. Alam, M. Qadir, M.A. Gafur, M. Moniruzzaman, Extraction and characterization of alumina nanopowders from aluminum dross by acid dissolution process, Int. J. Miner. Metall. Mater. 22 (2015) 429–436.

[43] A. Gil, S.A. Korili, Management and valorization of aluminum saline slags: current status and future trends, Chem. Eng. J. 289 (2016) 74–84, https://doi.org/10.1016/j.cej.2015.12.069.

[44] B. Dash, B.R. Das, B. Tripathy, I. Bhattacharya, S.C. Das, Acid dissolution of alumina from waste aluminium dross, Hydrometallurgy (2008) 48–53, https://doi.org/10.1016/j.hydromet.2008.01.006.

[45] B.R. Das, B. Dash, B.C. Tripathy, I.N. Bhattacharya, S.C. Das, Production of η-alumina from waste aluminium dross, Miner. Eng. 20 (2007) 252–258, https://doi.org/10.1016/j.mineng.2006.09.002.

[46] E.A. El-Katatny, S.A. Halawy, M.A. Mohamed, M.I. Zaki, Surface composition, charge and texture of active alumina powders recovered from aluminum dross tailings chemical waste, Powder Technol. 132 (2003) 137–144, https://doi.org/10.1016/S0032-5910(03)00047-0.

[47] H. Park, H. Lee, J. Kim, E. Yoon, A processing for recycling of the domestic aluminum, in: Dross, in: Glob. Symp. Recycl. Waste Treat. Clean Technol., REWAS, San Sebastian Spain, 1999, p. 995.

[48] J.J. Torrez-Herrera, E.G. Fuentes-Ordoñez, S.A. Korili, A. Gil, Evidence for the synthesis of La-hexaaluminate from aluminum-containing saline slag wastes: correction of structural defects and phase purification at low temperature, Powder Technol. 377 (2021) 80–88, https://doi.org/10.1016/j.powtec.2020.08.087.

[49] J.J. Torrez-Herrera, S.A. Korili, A. Gil, Structure and activity of nickel supported on hibonite-type La-hexaaluminates synthesized from aluminum saline slags for the dry reforming of methane, Chem. Eng. J. Adv. 5 (2021), 100080, https://doi.org/10.1016/j.ceja.2020.100080.

[50] J.J. Torrez-Herrera, S.A. Korili, A. Gil, Bimetallic (Pt-Ni) La-hexaaluminate catalysts obtained from aluminum saline slags for the dry reforming of methane, Chem. Eng. J. 433 (2022), 133191, https://doi.org/10.1016/j.cej.2021.133191.

[51] C. Belviso, A. Kharchenko, E. Agostinelli, F. Cavalcante, D. Peddis, G. Varvaro, N. Yaacoub, S. Mintova, Red mud as aluminium source for the synthesis of magnetic zeolite, Microporous Mesoporous Mater. 270 (2018), https://doi.org/10.1016/j.micromeso.2018.04.038.

[52] S. Kuroki, T. Hashishin, T. Morikawa, K. Yamashita, M. Matsuda, Selective synthesis of zeolites A and X from two industrial wastes: crushed stone powder and aluminum ash, J. Environ. Manag. 231 (2019) 749–756, https://doi.org/10.1016/j.jenvman.2018.10.082.

[53] M. Yoldi, E.G. Fuentes-Ordoñez, S.A. Korili, A. Gil, Zeolite synthesis from aluminum saline slag waste, Powder Technol. 366 (2020) 175–184, https://doi.org/10.1016/j.powtec.2020.02.069.

[54] R. Sánchez-Hernández, A. López-Delgado, I. Padilla, R. Galindo, S. López-Andrés, One-step synthesis of NaP1, SOD and ANA from a hazardous aluminum solid waste, Microporous Mesoporous Mater. 226 (2016) 267–277, https://doi.org/10.1016/j.micromeso.2016.01.037.

[55] A. Jiménez, A. Misol, Á. Morato, V. Rives, M.A. Vicente, A. Gil, Synthesis of pollucite and analcime zeolites by recovering aluminum from a saline slag, J. Clean. Prod. 297 (2021), 126667, https://doi.org/10.1016/j.jclepro.2021.126667.

[56] A. López-Delgado, F. López, L. Delgado, S. López-Andrés, F.J. Priego, Study by DTA/TG of the formation of calcium aluminate obtained from an aluminium hazardous waste, J. Therm. Anal. Calorim. 99 (2010), https://doi.org/10.1007/s10973-009-0597-z.

[57] A. López-Delgado, H. Tayibi, C. Pérez, F.J. Alguacil, F.A. López, A hazardous waste from secondary aluminium metallurgy as a new raw material for calcium aluminate glasses, J. Hazard. Mater. 165 (2009) 180–186, https://doi.org/10.1016/j.jhazmat.2008.09.124.

[58] E. Ewais, N.M. Khalil, M. Amin, Y. Ahmed, M. Barakat, Utilization of aluminum sludge and aluminum slag (dross) for the manufacture of calcium aluminate cement, Ceram. Int. 35 (2009) 3381–3388, https://doi.org/10.1016/j.ceramint.2009.06.008.

[59] R. Galindo, A. López-Delgado, I. Padilla, M. Yates, Hydrotalcite-like compounds: a way to recover a hazardous waste in the aluminium tertiary industry, Appl. Clay Sci. 95 (2014) 41–49, https://doi.org/10.1016/j.clay.2014.03.022.

[60] L. Santamaría, M. López-Aizpún, M. García-Padial, M.A. Vicente, S.A. Korili, A. Gil, Zn-Ti-Al layered double hydroxides synthesized from aluminum saline slag wastes as efficient drug adsorbents, Appl. Clay Sci. 187 (2020), 105486, https://doi.org/10.1016/j.clay.2020.105486.

[61] R. Galindo, A. López-Delgado, I. Padilla, M. Yates, Synthesis and characterisation of hydrotalcites produced by an aluminium hazardous waste: a comparison between the use of ammonia and the use of triethanolamine, Appl. Clay Sci. 115 (2015) 115–123, https://doi.org/10.1016/j.clay.2015.07.032.

[62] A. Gil, E. Arrieta, M.A. Vicente, S.A. Korili, Synthesis and CO_2 adsorption properties of hydrotalcite-like compounds prepared from aluminum saline slag wastes, Chem. Eng. J. 334 (2018) 1341–1350, https://doi.org/10.1016/j.cej.2017.11.100.

[63] L. Santamaría, M.A. Vicente, S.A. Korili, A. Gil, Saline slag waste as an aluminum source for the synthesis of Zn–Al–Fe–Ti layered double-hydroxides as catalysts for the photodegradation of emerging contaminants, J. Alloys Compd. 843 (2020), 156007.

[64] L. Santamaria, F. Devred, E.M. Gaigneaux, M.A. Vicente, S.A. Korili, A. Gil, Effect of the surface properties of Me^{2+}/Al layered double hydroxides synthesized from aluminum saline slag wastes on the adsorption removal of drugs, Microporous Mesoporous Mater. 309 (2020), 110560.

[65] J. Kim, K. Biswas, K.-W. Jhon, S.-Y. Jeong, W.-S. Ahn, Synthesis of $AlPO_4$-5 and CrAPO-5 using aluminum dross, J. Hazard. Mater. 169 (2009) 919–925, https://doi.org/10.1016/j.jhazmat.2009.04.035.

[66] N. Murayama, N. Okajima, S. Yamaoka, H. Yamamoto, J. Shibata, Hydrothermal synthesis of $AlPO_4$-5 type zeolitic materials by using aluminum dross as a raw material, J. Eur. Ceram. Soc. 26 (2006) 459–462, https://doi.org/10.1016/j.jeurceramsoc.2005.06.022.

[67] Y. Cardona, S.A. Korili, A. Gil, A nonconventional aluminum source in the production of alumina-pillared clays for the removal of organic pollutants by adsorption, Chem. Eng. J. 425 (2021), 130708, https://doi.org/10.1016/j.cej.2021.130708.

[68] J. Zhang, B. Liu, S. Zhao, H. Shen, J. Liu, S. Zhang, Preparation and characterization of glass ceramic foams based on municipal solid waste incineration ashes using secondary aluminum ash as foaming agent, Constr. Build. Mater. 262 (2020), 120781, https://doi.org/10.1016/j.conbuildmat.2020.120781.

[69] M. Wang, S. Xu, Preparation and applications of foam ceramics, IOP Conf. Ser. Earth Environ. Sci. 186 (2018), https://doi.org/10.1088/1755-1315/186/2/012066.

[70] M.V. Twigg, J.T. Richardson, Fundamentals and applications of structured ceramic foam catalysts, Ind. Eng. Chem. Res. 46 (2007) 4166–4177, https://doi.org/10.1021/ie061122o.

[71] H. Haugen, J. Will, A. Köhler, U. Hopfner, J. Aigner, E. Wintermantel, Ceramic TiO2-foams: characterisation of a potential scaffold, J. Eur. Ceram. Soc. 24 (2004) 661–668, https://doi.org/10.1016/S0955-2219(03)00255-3.

[72] M. Takahashi, R.L. Menchavez, M. Fuji, H. Takegami, Opportunities of porous ceramics fabricated by gelcasting in mitigating environmental issues, J. Eur. Ceram. Soc. 29 (2009) 823–828, https://doi.org/10.1016/j.jeurceramsoc.2008.07.030.

[73] S. Vijayan, P. Wilson, K. Prabhakaran, Porosity and cell size control in alumina foam preparation by thermo-foaming of powder dispersions in molten sucrose, J. Asian Ceramic Soc. 4 (2016) 344–350, https://doi.org/10.1016/j.jascer.2016.06.007.

[74] R. Faure, F. Rossignol, T. Chartier, C. Bonhomme, A. Maître, G. Etchegoyen, P. Del Gallo, D. Gary, Alumina foam catalyst supports for industrial steam reforming processes, J. Eur. Ceram. Soc. 31 (2011) 303–312, https://doi.org/10.1016/j.jeurceramsoc.2010.10.009.

[75] J. Saggio-Woyansky, C.E. Scott, W.P. Minnear, Processing of porous ceramics, Am. Ceram. Soc. Bull. 71 (1992) 1674–1682.

[76] X. Li, Y. Li, R. Xiang, S. Li, Q. Zhou, H. Luo, Fabrication of ultra-high-porosity cordierite foams by the thermo-foaming of powder dispersions in molten D-glucose anhydrous, J. Mater. Res. 34 (2019) 1818–1825, https://doi.org/10.1557/jmr.2019.13.

[77] R. Narasimman, K. Prabhakaran, Preparation of low density carbon foams by foaming molten sucrose using an aluminium nitrate blowing agent, Carbon N. Y. 50 (2012) 1999–2009, https://doi.org/10.1016/j.carbon.2011.12.058.

[78] S. Vijayan, R. Narasimman, C. Prudvi, K. Prabhakaran, Preparation of alumina foams by the thermo-foaming of powder dispersions in molten sucrose, J. Eur. Ceram. Soc. 34 (2014) 425–433, https://doi.org/10.1016/j.jeurceramsoc.2013.08.023.

[79] M.A. Alves-Rosa, L. Martins, S.H. Pulcinelli, C.V. Santilli, Design of microstructure of zirconia foams from the emulsion template properties, Soft Matter 9 (2013) 550–558, https://doi.org/10.1039/c2sm26842f.

[80] S. Barg, E.G. de Moraes, D. Koch, G. Grathwohl, New cellular ceramics from high alkane phase emulsified suspensions (HAPES), J. Eur. Ceram. Soc. 29 (2009) 2439–2446, https://doi.org/10.1016/j.jeurceramsoc.2009.02.003.

[81] B.P. Binks, T.S. Horozov, Aqueous foams stabilized solely by silica nanoparticles, Angew. Chem. Int. Ed. 44 (2005) 3722–3725, https://doi.org/10.1002/anie.200462470.

[82] U.T. Gonzenbach, A.R. Studart, E. Tervoort, L.J. Gauckler, Ultrastable particle-stabilized foams, Angew. Chem. Int. Ed. 45 (2006) 3526–3530, https://doi.org/10.1002/anie.200503676.

[83] F.S. Ortega, P. Sepulveda, V.C. Pandolfelli, Monomer systems for the gelcasting of foams, J. Eur. Ceram. Soc. 22 (2002) 1395–1401, https://doi.org/10.1016/S0955-2219(01)00486-1.

[84] J.G.P. Binner, Production and properties of low density engineering ceramic foams, Br. Ceram. Trans. 96 (1997) 247–249. https://www.scopus.com/inward/record.uri?eid=2-s2.0-0031365148&partnerID=40&md5=be6d2506cd6c6a73215c16f380d95553.

[85] U. Soy, A. Demir, F. Caliskan, Effect of bentonite addition on fabrication of reticulated porous SiC ceramics for liquid metal infiltration, Ceram. Int. 37 (2011) 15–19.

[86] P.J. Beldon, L. Fábián, R.S. Stein, A. Thirumurugan, A.K. Cheetham, T. Friščić, Rapid room-temperature synthesis of zeolitic imidazolate frameworks by using mechanochemistry, Angew. Chem. Int. Ed. 49 (2010) 9640–9643, https://doi.org/10.1002/anie.201005547.

[87] J. Cravillon, S. Münzer, S.-J. Lohmeier, A. Feldhoff, K. Huber, M. Wiebcke, Rapid room-temperature synthesis and characterization of nanocrystals of a prototypical zeolitic imidazolate framework, Chem. Mater. 21 (2009) 1410–1412, https://doi.org/10.1021/cm900166h.

[88] J.A. Thompson, K.W. Chapman, W.J. Koros, C.W. Jones, S. Nair, Sonication-induced Ostwald ripening of ZIF-8 nanoparticles and formation of ZIF-8/polymer composite membranes, Microporous Mesoporous Mater. 158 (2012) 292–299, https://doi.org/10.1016/j.micromeso.2012.03.052.

[89] S. Garcés-Polo, J. Villarroel-Rocha, K. Sapag, S.A. Korili, A. Gil, Comparative study of the adsorption equilibrium of CO_2 on microporous comercial materials at low pressures, Ind. Eng. Chem. Res. 52 (2013) 6785–6793, https://doi.org/10.1021/ie400380w.